

UNCLASSIFIED

---

AD 400 472

*Reproduced  
by the*

ARMED SERVICES TECHNICAL INFORMATION AGENCY  
ARLINGTON HALL STATION  
ARLINGTON 12, VIRGINIA



---

UNCLASSIFIED

NOTICE: When government or other drawings, specifications or other data are used for any purpose other than in connection with a definitely related government procurement operation, the U. S. Government thereby incurs no responsibility, nor any obligation whatsoever; and the fact that the Government may have formulated, furnished, or in any way supplied the said drawings, specifications, or other data is not to be regarded by implication or otherwise as in any manner licensing the holder or any other person or corporation, or conveying any rights or permission to manufacture, use or sell any patented invention that may in any way be related thereto.

63-3-1

CATALOGED BY ASTIA 400472  
AS AD NO. \_\_\_\_\_

ASD-TDR-62-431

# DISLOCATION MOBILITY AND PINNING IN HARD MATERIALS THROUGH INTERNAL FRICTION STUDIES

TECHNICAL DOCUMENTARY REPORT NO. ASD-TDR-62-431

February 1963

Directorate of Materials and Processes  
Aeronautical Systems Division  
Air Force Systems Command  
Wright-Patterson Air Force Base, Ohio

Project No. 7350, Task No. 735003



(Prepared under Contract No. AF 33(616)-8132 by the Armour  
Research Foundation, Chicago, Illinois; P. D. Southgate, author.)

UNCLASSIFIED

## NOTICES

When Government drawings, specifications, or other data are used for any purpose other than in connection with a definitely related Government procurement operation, the United States Government thereby incurs no responsibility nor any obligation whatsoever; and the fact that the Government may have formulated, furnished, or in any way supplied the said drawings, specifications, or other data, is not to be regarded by implication or otherwise as in any manner licensing the holder or any other person or corporation, or conveying any rights or permission to manufacture, use, or sell any patented invention that may in any way be related thereto.

Qualified requesters may obtain copies of this report from the Armed Services Technical Information Agency, (ASTIA), Arlington Hall Station, Arlington 12, Virginia.

This report has been released to the Office of Technical Services, U.S. Department of Commerce, Washington 25, D.C., in stock quantities for sale to the general public.

Copies of this report should not be returned to the Aeronautical Systems Division unless return is required by security considerations, contractual obligations, or notice on a specific document.

## FOREWORD

This report was prepared by the Armour Research Foundation of the Illinois Institute of Technology under USAF Contract No. AF 33(616)-8132. This contract was initiated under Project No. 7350, "Refractory Inorganic Nonmetallic Materials", Task No. 735003, "Theory and Mechanical Phenomena". The work was administered under the direction of the Directorate of Materials and Processes, Deputy for Technology, Aeronautical Systems Division, with Mr. George W. King acting as project engineer.

This report covers work conducted during the period April 1, 1961 to March 31, 1962.

Personnel employed in the investigation were P. D. Southgate and A. E. Attard. D. K. Benson assisted with the design and construction of the apparatus.

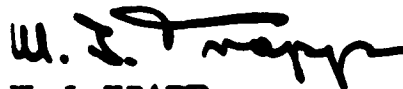
## ABSTRACT

The internal friction of covalently bonded and partly covalently bonded materials is being investigated at elevated temperatures. The apparatus operates on the electrostatic drive system, and covers the range 0 to 1500°C, 1 to 200 kc/s. Single crystals of silicon, silicon carbide, and zinc oxide have been measured. A steady rise of internal friction is seen in deformed silicon specimens above 500°C, which appears to be thermally activated with an activation energy of  $1.61 \pm 0.02$  eV. The rise is attributed to the dislocation damping; its magnitude is approximately proportional to the dislocation density and inversely to the frequency. Quantitative identification can be made with Brailsford's abrupt-kink theory of dislocation damping if a reasonable kink density is assumed, in which case the activation energy is that of kink mobility.

Observations of creep rate during deformation of silicon crystals at 950°C give rather variable results. The most common situation is that of approximately logarithmic creep, followed by some work hardening. Deviations occur in the form of an incubation time for creep, of a continuously increasing creep rate. Specimen orientation and oxygen content did not seem to have a major effect on behavior.

Silicon carbide and zinc oxide were measured only in the undeformed state. A number of peaks were seen in zinc oxide (29 kc/s) at 135°, 190° and 345°C, and in silicon carbide (110 kc/s) at 500°C. Rapid rises in internal friction occurred above 750° in zinc oxide and 900° in silicon carbide. The peaks are too wide to be caused by simple point defect relaxation, and further data are required to identify them. The general annealing behavior of the rise in silicon carbide is very similar to that in an anomalous silicon specimen having a very non-uniform dislocation distribution.

This report has been reviewed and is approved.



W. J. TRAPP  
Chief, Strength and Dynamics Branch  
Metals and Ceramics Laboratory  
Directorate of Materials and Processes

## TABLE OF CONTENTS

	Page
I     INTRODUCTION . . . . .	1
II    GENERAL DISCUSSION . . . . .	1
III   INTERNAL FRICTION APPARATUS . . . . .	6
MEASUREMENT TECHNIQUE . . . . .	6
FURNACE AND SPECIMEN SUPPORT:	
UNIT 1 . . . . .	8
ELECTRONIC CIRCUITS . . . . .	12
OPERATION OF SYSTEM . . . . .	21
GRID CAPACITANCE CHANGE . . . . .	24
IV    SPECIMEN PREPARATION . . . . .	26
FORM OF SPECIMEN . . . . .	26
ORIGIN AND NATURE OF MATERIAL . . . . .	28
V     DEFORMATION OF SILICON . . . . .	30
APPARATUS . . . . .	30
CREEP CURVES . . . . .	34
DISLOCATION DISTRIBUTION . . . . .	37
VI    INTERNAL FRICTION OF SILICON . . . . .	45
EXPERIMENTAL RESULTS . . . . .	45
APPLICABILITY OF SDP AND BRAILSFORD	
THEORIES . . . . .	54
VII   INTERNAL FRICTION OF SILICON CARBIDE . . . . .	59
VIII   INTERNAL FRICTION OF ZINC OXIDE . . . . .	63
IX    ELASTIC MODULI . . . . .	67
X     CONCLUSION . . . . .	70

**TABLE OF CONTENTS (Continued)**

	<b>Page</b>
<b>APPENDIX I - FORCE AND ENERGY RELATIONSHIPS FOR A DISLOCATION CONTAINING KINKS . . .</b>	<b>72</b>
<b>APPENDIX II - DISLOCATION LINE TENSION IN THE BRAILSFORD THEORY . . . . .</b>	<b>74</b>
<b>APPENDIX III - COMPARISON OF KINK REPULSION AND STRESS-FIELD LINE TENSION MODELS . . .</b>	<b>79</b>
<b>APPENDIX IV - MODIFICATION OF BRAILSFORD THEORY: STRESS-FIELD ENHANCED KINK DIFFUSION . . . . .</b>	<b>81</b>
<b>APPENDIX V - COMPATIBILITY OF BRAILSFORD AND KGL THEORIES . . . . .</b>	<b>84</b>



## LIST OF ILLUSTRATIONS

Figure		Page
1	Photograph of Drive Grid . . . . .	7
2	Block Diagram of Apparatus . . . . .	9
3	Photograph of Apparatus . . . . .	10
4	Section of Furnace and Specimen Mount . . . . .	11
5	Circuit of Discriminator-Amplifier . . . . .	13
6	Discriminator Curve . . . . .	14
7	Drive Amplifier . . . . .	16
8	High-Stability Generator . . . . .	17
9	Frequency Divider . . . . .	18
10	Detector Circuit . . . . .	20
11	Plug Interchange . . . . .	22
12	Detector Curve . . . . .	23
13	Sequence of Bending and Cutting Dumbbell Specimen . .	27
14	Apparatus for Bending Silicon Bars . . . . .	31
15	Apparatus for Bending Silicon Bars; Semi-Diagrammatic Section . . . . .	32
16	Creep Curves of Silicon Specimens . . . . .	35
17	Dislocation Pattern in Silicon 2043 . . . . .	38
18	Dislocation Pattern in Silicon 2033 . . . . .	39
19	Dislocation Pattern in Silicon 2044 . . . . .	40
20	Etch Pit Distribution in 2043 . . . . .	42
21	Etch Pit Distribution in 2044 . . . . .	43
22	Internal Friction of Silicon 2031 . . . . .	46
23	Internal Friction of Silicon 2034 . . . . .	47

# LIST OF ILLUSTRATIONS (Continued)

Figure		Page
24	Internal Friction of Silicon 2043 . . . . .	48
25	Internal Friction of Silicon 2042 . . . . .	49
26	Internal Friction of Silicon 2042: Derived Dislocation Damping Curves. . . . .	50
27	Internal Friction of Silicon 2044 . . . . .	51
28	Internal Friction of Silicon 2032 . . . . .	52
29	Internal Friction of Silicon 2033 . . . . .	55
30	Internal Friction of Silicon 2033: Showing Heating and Cooling Sequence . . . . .	56
31	Internal Friction of Silicon Carbide 3104: High Temperature Rise. . . . .	60
32	Internal Friction of Silicon Carbide 3104: Lower Temperature Variation . . . . .	61
33	Internal Friction of Silicon Carbide 3104: 500°C Peak .	62
34	Internal Friction of Zinc Oxide . . . . .	65
35	Temperature Variation of Elastic Modulus: Silicon, Silicon Carbide, Zinc Oxide, Magnesium Oxide . . . . .	69
36	Kinked Dislocation Showing Core and Stress-Field Regions . . . . .	73

## LIST OF TABLES

Table		Page
1	ANALYSIS OF CHIEF IMPURITIES IN SiC SPECIMEN 310 (WEIGHT PERCENTAGES) . . . . .	29
2	DATA ON DEFORMED SPECIMENS . . . . .	36
3	DISLOCATION DAMPING IN SILICON . . . . .	53

## Section I

### INTRODUCTION

This is the final report on work carried out under Contract No. AF33(616)-8132 over the period April 1961 to March 1962. It concerns studies of dislocation motion and diffusion of defects in the covalently bonded materials silicon, silicon carbide, and zinc oxide, using internal friction methods. The high temperature mechanical properties of these materials have been as yet investigated only incompletely, and the data on defect motion obtained from internal friction studies should be of considerable assistance in understanding such processes as creep, fatigue, and fracture.

Usually, a number of variable parameters are involved in any particular internal friction mechanism, and the deduction of the detailed nature of the mechanism requires a careful control over these parameters. Of the three materials investigated, silicon is by far the most controllable at present. It is obtainable either of high purity or with exactly known impurity contents, its dislocation content can be readily measured by etch-pit techniques, and the question of non-stoichiometry does not arise. Hence the major work of the report has been concerned with silicon. Having established the behavior of the material, it will be easier to analyze observations on zinc oxide and silicon carbide, which have analogous though not identical structures. This objective, of comparing similar processes in the three materials, has not been achieved during the first year of investigation, since the dominant effects observed in zinc oxide and silicon carbide have been almost certainly different from those in silicon. Effective techniques for uniformly introducing dislocations into silicon have been developed, and the main process studied has been a mechanism of dislocation damping which is intrinsic to the pure material; while the other two materials have been measured in the as-grown condition, and the major source of loss has probably been due to impurities.

## Section II

### GENERAL DISCUSSION

The measure of internal friction, or mechanical damping, used in this report is the logarithmic decrement  $\Delta$ . It is related to other measures of internal friction by

---

Manuscript released by the author March 1962 for publication as an ASD Technical Documentary Report.

$$\Delta = \pi/Q = \lambda\gamma = \frac{\delta E}{2E}$$

Q being the mechanical Q factor,  $\gamma$  the acoustic attenuation factor,  $\lambda$  the wavelength of sound,  $\delta E$  the energy loss per cycle, and  $E$  the total mechanical energy of the specimen. When the internal friction is low,  $\Delta$  is also equal to the mechanical loss angle multiplied by  $\pi$ .

A very brief resume of the elements of the theory of defect relaxation will now be given.

Most internal friction mechanisms are governed by relaxation processes, typified by a relaxation time, or range of relaxation times. The relaxation process gives a small strain additional to the normal elastic strain, so that the total strain is

$$\epsilon = \sigma/M + \epsilon_2$$

where  $M$  is the elastic modulus. The particular circumstances will determine the appropriate modulus: for dislocation motion along a slip plane, it will be the shear modulus.

The relaxation of the strain is determined by

$$\frac{d\epsilon_2}{dt} = - \frac{\epsilon_2 - \epsilon_{20}}{\tau}$$

where  $\epsilon_{20}$  is the ultimate extent of the relaxation, and  $\tau$  the relaxation time. Hence, for sinusoidal motion,

$$\epsilon_2 = \frac{\epsilon_{20}}{1 + j\omega\tau}$$

If we put  $\epsilon_{20}$  proportional to the applied stress amplitude, so that  $\epsilon_{20} = \alpha\sigma$ , then

$$\epsilon = \sigma \left( \frac{1}{G} + \frac{a}{1 + j\omega\tau} \right)$$

When  $aG$  is small,  $\Delta$  will be equal to the loss angle, which is the ratio of the imaginary to the real parts of the expression on the right hand side.

$$\Delta = aG \frac{\omega\tau}{1 + \omega^2\tau^2} \quad (2.1)$$

In general, if a range of relaxation times is involved

$$\Delta = G \sum_r \frac{a_r \omega \tau_r}{1 + \omega^2 \tau_r^2} \quad (2.2)$$

Thus, a plot of internal friction against frequency shows a series of relaxation peaks, having a maximum  $\Delta_m = aG/2$  when  $\omega\tau = 1$ . If, in addition, the relaxation process is thermally activated, then the relaxation time will have a temperature dependence of the form

$$\tau = \tau_0 \exp (H/kT) \quad (2.3)$$

$H$  being an activation energy. In this case a plot of internal friction against temperature will also show a series of relaxation peaks. It is usually more convenient to make a temperature plot rather than a frequency plot.

Relaxation processes which are amenable to study by internal friction methods include those of impurity motion, dislocation motion,

thermoelastic damping,<sup>1</sup> and electroacoustic damping.<sup>2,3</sup> For the materials studied in this report, thermoelastic damping is usually small, and the electroacoustic damping probably plays no part. For impurities to produce damping, they must be situated in a site of lower symmetry than the crystal lattice. Such a condition holds for many interstitial atoms, and for atom pairs, or atoms with associated vacancies. The best-known example of this is carbon in  $\alpha$ -iron, giving the very clear-cut relaxation known as the Snoek peak.<sup>4</sup> Impurity relaxation usually gives a peak close to the form given by equations (2.1) and (2.3). The factor  $\alpha$  is then determined by the change in crystal distortion produced by the hopping of the impurity between the non-equivalent sites. In silicon, the only impurity present in sufficient concentrations to produce measurable internal friction is interstitial oxygen. The relaxation of this defect has already been studied,<sup>5</sup> and it is known that, for a specimen vibrating in a  $[100]$  direction, no damping is produced since all possible sites are equivalently located with respect to  $[100]$ . Hence, in the present study, those specimens in which it is desired to measure the effect of oxygen on dislocation damping without the obscuring effect of the oxygen relaxation itself are measured in the  $[100]$  direction.

Dislocation relaxation involves a more complicated situation than impurity relaxation, since a wide range of dislocation lengths is involved, and since the detailed geometry of the dislocation is usually not fully understood. It is this understanding of the importance of dislocation geometry to the relaxation which has been one of the major concerns of the present investigation. The majority of work published on dislocation relaxation has been on the Bordoni peak<sup>6</sup> in metals, which lies below room temperature, and which is broader than a simple relaxation peak. Two theories have been put forward to explain the peak, that of Seeger, Donth and Pfaff<sup>7</sup> (SDP theory) and that of Brailsford.<sup>8</sup> In general, dislocation damping theories differ in the extent to which the discrete nature of the lattice affects dislocation motion and configuration. Both the SDP and Brailsford theories take the situation when dislocations are predominantly held in the lattice potential wells which form the Peierls force. The dislocations then move from one to the other by the lateral motion of kinks. In the SDP theory the kinks move freely, whereas in the Brailsford theory they have a finite mobility originating in the need for thermal excitation from one atom position to the next. It is not clear which situation applies to the Bordoni peak in metals. The two theories will be discussed further in Section VI and in the appendices, and evidence will be adduced for the applicability of the Brailsford theory to high temperature relaxation in silicon. Higher temperatures are required for this process compared with the probably analogous low-temperature Bordoni peak in metals because the bonding in silicon is stiffer and more directional, and hence higher thermal energies are required to maintain kink mobility.

When the Peierls force becomes of secondary importance, then the motion of a dislocation is determined by three main factors: a line

tension due to its elastic stress field, its effective mass, and a damping force which may or may not reflect the discrete nature of the lattice. Under these conditions the theory of Granato and Lucke<sup>9</sup> based on the dislocation damping equation of Koehler<sup>10</sup> (KGL theory) is applicable. Two peaks in internal friction as a function of frequency are seen. One occurs at very high frequencies, is only seen when damping is very small, and is due to elastic resonance of the dislocation; the other is a relaxation peak with a relaxation time  $\ell^2 B / \pi^2 E_0$ , where  $\ell$  is the dislocation length,  $B$  the damping constant, and  $E_0$  the energy per unit length of the dislocation stress-field. A distribution of lengths gives a distribution of relaxation time, which broadens the peak. If the damping constant  $B$  contains a thermal activation factor, then the KGL theory leads to a Bordoni peak. Compatibility of the KGL theory with the Brailsford theory is discussed in Appendix 5.

The most significant process which is not a relaxation process is that of dislocation break-away. Granato and Lucke have given the theory of this process also.<sup>9</sup> It is characterized by a lack of frequency dependence, and a marked amplitude dependence of damping. Some samples of silicon and silicon carbide appear to show behavior of this type, although the behavior appears to be very unstable. In general, the fit of predicted amplitude dependence with that observed is not very satisfactory, and modification of the theory is required. Swartz and Weertman<sup>11</sup> have developed a modification suitable for bcc metals, where some impurities interact only with the edge components of dislocations, while others interact both with edge and screw components. This situation probably does not apply in the diamond or zinc blende structure.



### Section III

## INTERNAL FRICTION APPARATUS

### MEASUREMENT TECHNIQUE

The materials which are to be measured have, at least at low temperatures, extremely low values of internal friction. This fact limits considerably the number of possible methods of measuring internal friction, since in any system utilizing direct mechanical coupling between a transducer and the specimen, the damping of the transducer would probably mask that of the specimen. The electrostatically coupled system first devised by Bordoni<sup>12, 13</sup> avoids this difficulty. For conducting specimens, a plate is placed a small distance from the specimen, and the drive potential (at the specimen resonant frequency) is applied between the plate and specimen. If the mechanical drive is to be of the same frequency as the applied electrical signal, it is necessary also to apply a biasing voltage somewhat greater than the applied voltage. In addition, motion of the specimen will change the capacitance of the gap; hence, if this is made part of a high-frequency tuned circuit connected to an oscillator (36 Mc/s in our case), a frequency modulated output proportional to the specimen displacement will be obtained.

Electrostatic drive forces, for conducting specimens, arise directly from the uniform field between the specimen and the drive plate. In the case of a dielectric specimen, a uniform field produced by this arrangement would yield no attractive force, and an inhomogeneous field is required. This is produced by the grid shown in Fig. 1. Two sets of bars are connected alternately to parallel wires across which the drive is applied. Near the surface of the grid, the field is very inhomogeneous and a dielectric specimen will be attracted toward it; the system works like a magnetic chuck. Similarly, motion of the dielectric towards or away from the grid surface will change the capacitance between the two sets of bars. An approximate theory of the magnitude of the effect is given in Section III, part 5.

There are several ways of obtaining values for internal friction. The most desirable, giving an instantaneous meter-reading value, is to compare drive power with the oscillation amplitude which is excited. Unfortunately, this is not applicable to electrostatic drive systems since the drive efficiency cannot be determined accurately. The resonance width can be used to determine  $Q$ , but this method is susceptible to drift. The method chosen is that of plotting the free decay curve of the specimen. The output from the 36 Mc/s oscillator is amplified and fed into a discriminator. After further amplification and mixing with a local oscillator the signal emerges at 2 kc/s with the decay envelope of the specimen oscillation. The signal is finally displayed on a logarithmic recorder, so that an exponential decay envelope appears

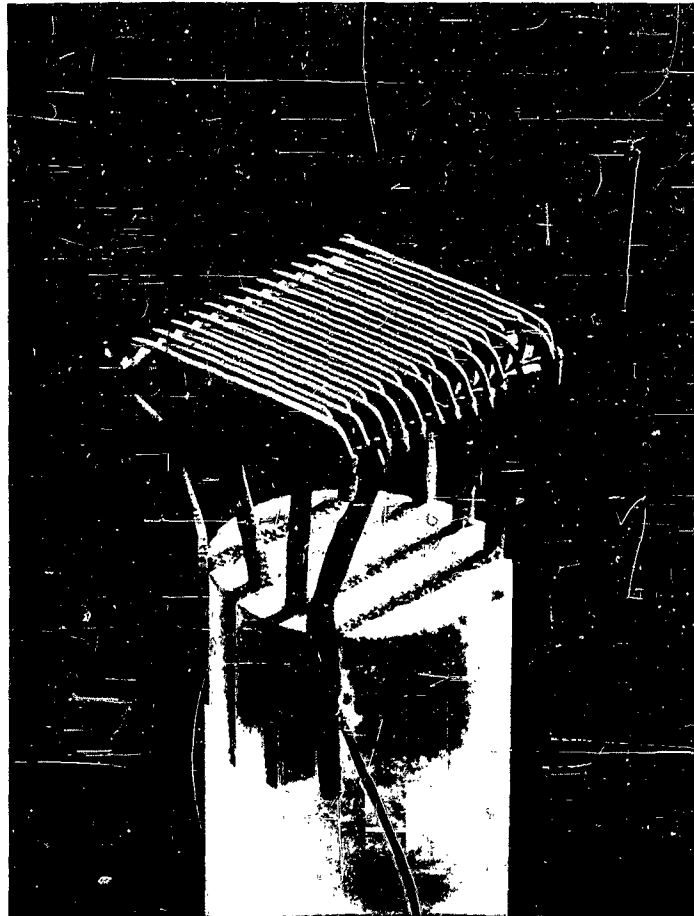


Fig. 1 - PHOTOGRAPH OF DRIVE GRID

as a straight line. Deviations from the exponential form, representing changes of internal friction with amplitude, can thus be readily detected.

A block diagram of the whole system is shown in Fig. 2. The drive generator is required to be of high stability so that the frequency may be held on the narrow specimen resonance, and so it consists of a main oscillator locked into a high-stability frequency meter oscillator. An oscilloscope displays the Lissajous figure of drive signal vs. specimen oscillation signal (before mixing) thus affording a sensitive means of detecting resonance.

A general view of the apparatus is shown in Fig. 3. The majority of the electronic circuits are contained in the rack at the left. The X-Y oscilloscope and the logarithmic recorder are on the bench. Further to the right appears the part of the apparatus containing the furnace, vacuum system, specimen and detecting oscillator ("the cart"), while the furnace supply rack is to the extreme right. The furnace is suspended by anti-vibration mounts; connection to the all-metal vacuum system is made via a flexible bellows tube.

#### FURNACE AND SPECIMEN SUPPORT: UNIT 1

The furnace is required to work in a vacuum, to reach temperature in excess of  $1500^{\circ}\text{C}$ , and to have a very short time constant to facilitate quenching experiments. A molybdenum tube furnace will satisfy such requirements. The construction is seen in section in Fig. 4. The furnace body, which acts as the vacuum envelope, is highly polished on the inside to reflect heat and is surrounded by a water jacket. The heating tube consists of a 0.002 in. molybdenum foil wrapped into a cylinder and clamped by end-rings, being held in tension by the spring and bellows arrangement in the furnace top cap. Potential is applied between the top cap and the body, an interposed O-ring acting both as vacuum seal and electrical insulation. With an input of 7.5 v, 240 A, a temperature of  $1400^{\circ}\text{C}$  is attained.

The specimen is shown in Fig. 4 supported so that it is excited into flexural oscillation. The grid is held close to the center section of the side, and the specimen supported by two fine tungsten wires passing through holes drilled through the nodal points. Screw adjustments on the base-plate hold the wires in tension across the top of a silica or ceramic tube, into which cross-bars have been fastened. The specimen is adjusted so the gap is parallel by bending the bars. For conducting specimens, the specimen is used as one drive electrode; otherwise the support wires are grounded. The ceramic support for the grid passes up the center of the tube, and a micrometer screw and lateral adjustments beneath the base-plate allow setting-up and calibration adjustments of the grid-specimen gap to be made.



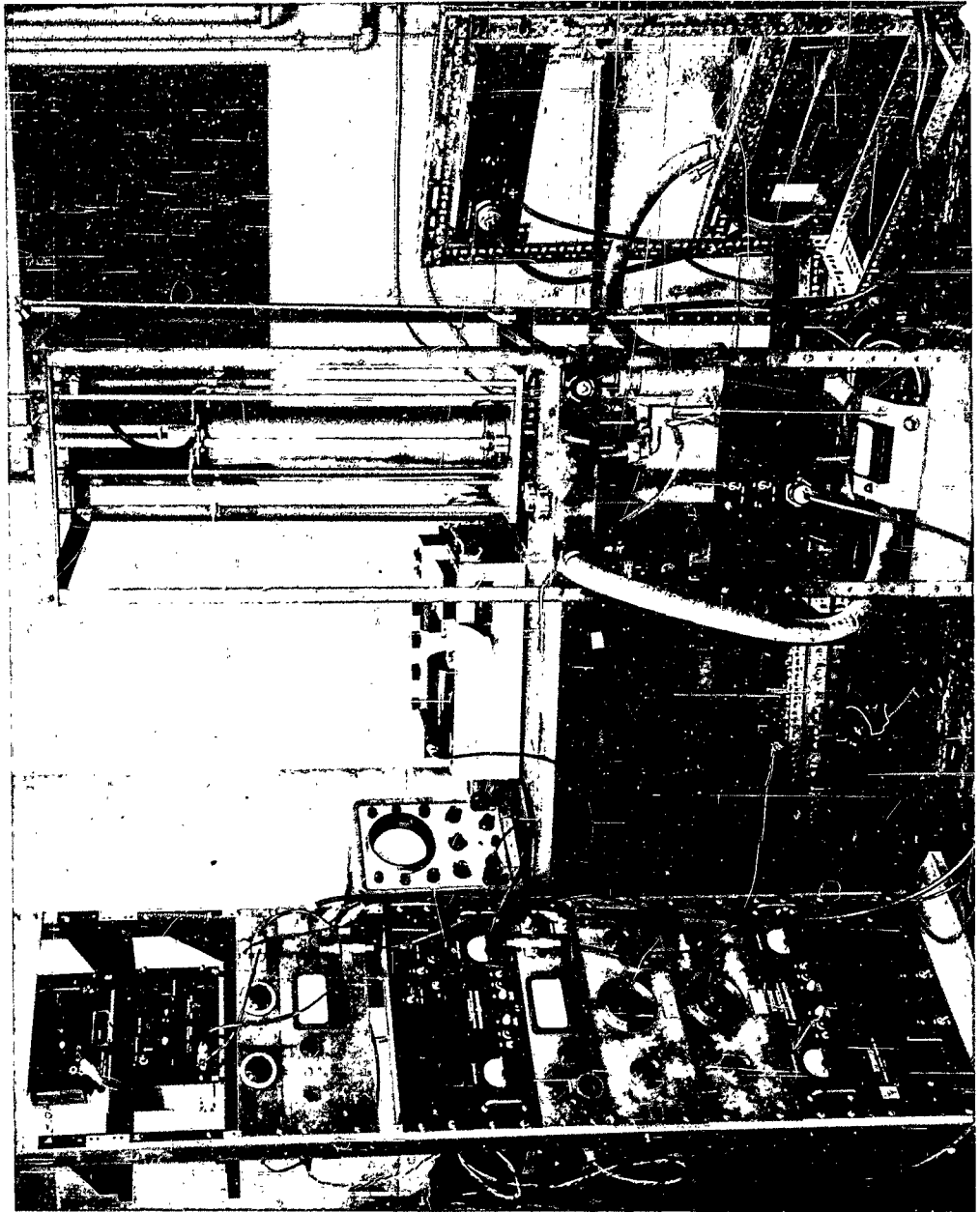
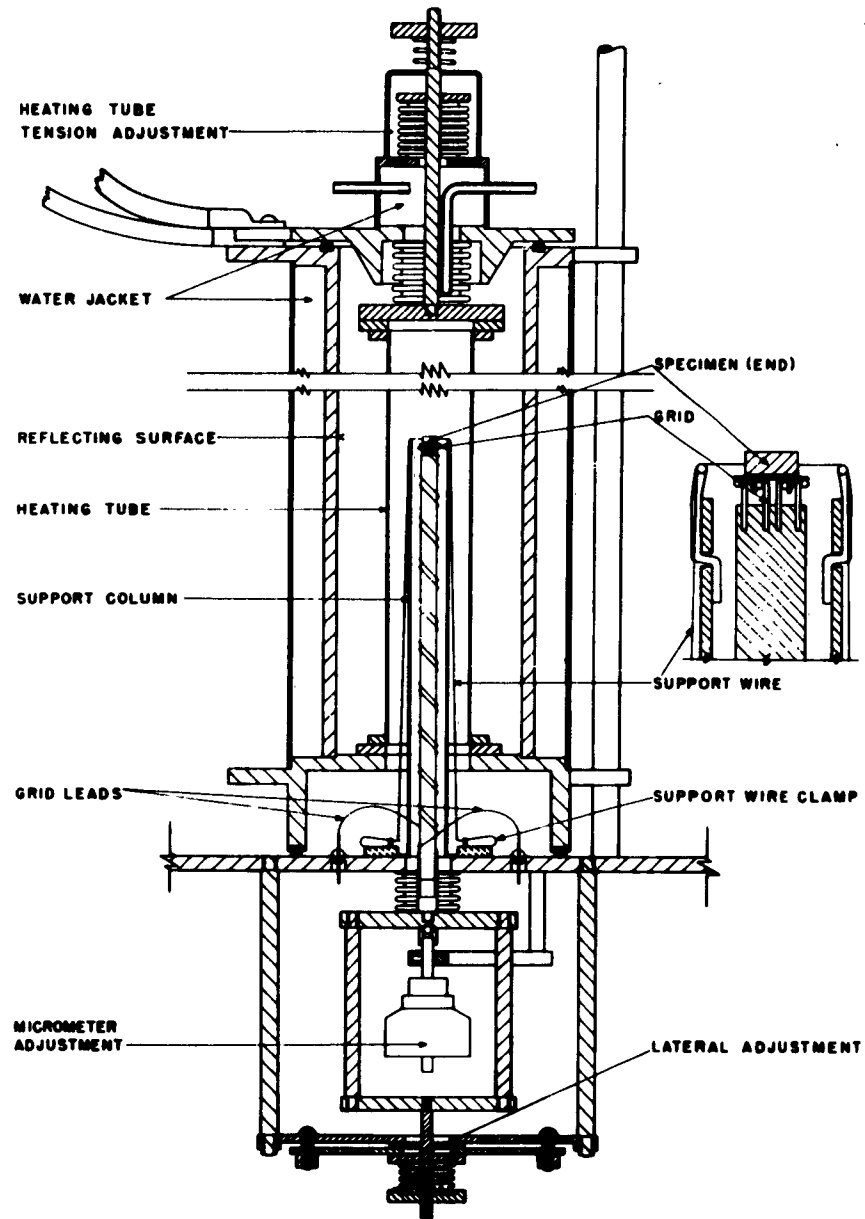


Fig. 3 - PHOTOGRAPH OF APPARATUS



**FIG. 4 - SECTION OF FURNACE AND SPECIMEN MOUNT**

Fabrication of the grid is a matter requiring some care. Molybdenum wires 0.01" in diameter are laid parallel, being separated by 0.005" diameter wire. Alternate wires are then spot-welded to either of two pairs of tantalum cross-bars, and the ends of the grid wires cut off. After bending so that the two sets of cross-bars are not in contact with the wires, the grid is spot-welded to wires fixed into the end of the ceramic support rod. The assembly is then set in epoxy resin, leaving the face exposed so that it can be polished flat to remove slight distortions. Finally, the resin is dissolved away.

## ELECTRONIC CIRCUITS

### Unit 2: Discriminator Amplifier

The circuit is shown in Fig. 5. The 36 Mc/s input enters at a level of about 1 volt, is amplified by the 6AK5 tube and is fed directly into the Foster-Seeley discriminator circuit in the tube anode circuit. The discriminator output is filtered ( $560\Omega$ ,  $47\mu F$ ) and travels via SW 1/2, shorted, to the first amplifier tube. The meter in the cathode measures the DC component of discriminator output, corresponding to the center frequency of the input signal. After filtering of low-frequency components, the signal passes to a mixer 6AU6 tube, which has a large additional signal, 2 kc/s higher than the amplified signal, applied to the cathode through SK 3/2. The anode circuit has variable band-width centered on 2 kc/s. The subsequent amplifier has more filtering to remove the local oscillator signal and 36 Mc/s leakage. Alternatively, SW 4/2 allows the amplifier to be used for a straight 1 to 10 kc/s amplification, since it is not possible to filter out local oscillator signal well enough below 10 kc/s. The final output to the recorder is from a cathode follower.

The discriminator response curve as indicated by the meter for an RF input of 1 v is shown in Fig. 6. The linear portion extends over 1.2 Mc/s showing that the maximum frequency of mechanical oscillation that can be measured accurately using the DC calibration is 600 kc/s. Undistorted decay curves will be obtained for higher frequencies, however.

The overall gain of the lower frequency amplifier-mixer circuit from the grid of the first 6CB6 to the output is  $1.3 \times 10^4$ ; the equivalent input voltage corresponding to noise and local oscillator break-through is 3  $\mu V$  at 50 kc/s. The amplifier gain can be checked by the calibrating networks on SW 1/2, SW 2/2 using a monitored signal of the drive frequency from Unit 3. Changing the switch to the calibrating positions puts a filter circuit in, which removes the AC component of discriminator output while retaining the DC bias so that the amplifier gain does not change.





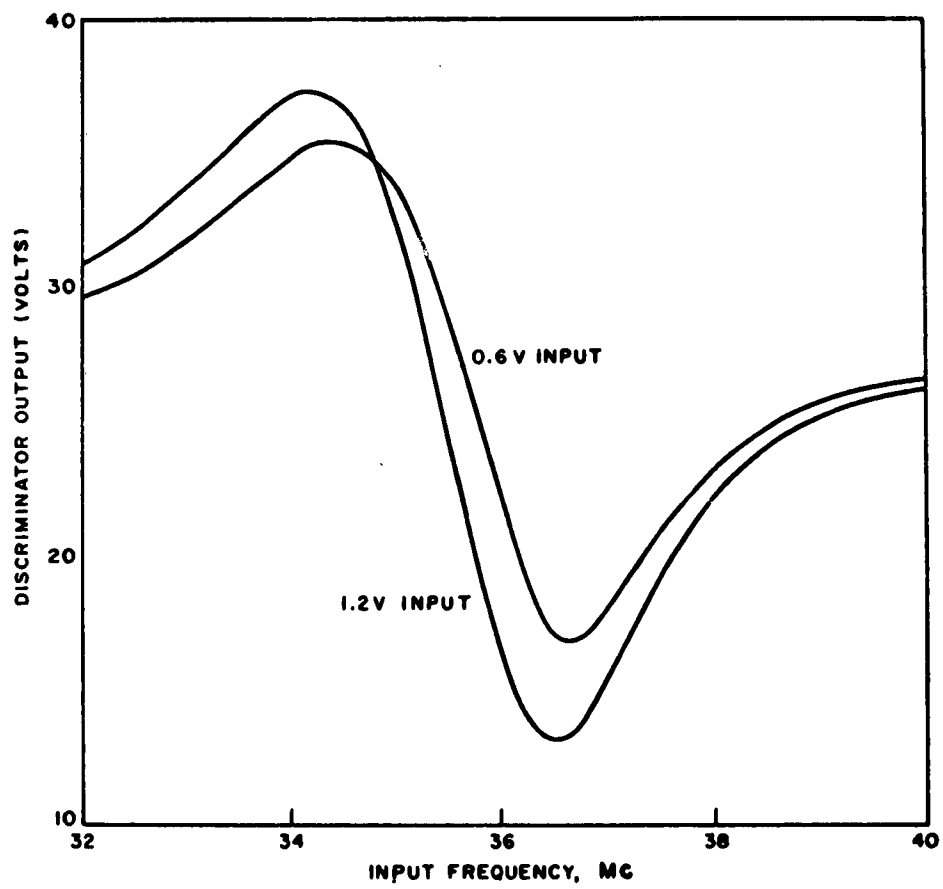


FIG. 6 - DISCRIMINATOR CURVE

### Unit 3: Drive Amplifier

The circuit is shown in Fig. 7. The input, varying from 1 kc/s to 200 kc/s at a level of approximately 1 v passes through one stage of untuned amplification before the final inductively loaded power stage. The tuning is broad and various bands are selected by SW 1/3. A maximum output voltage of 180 v RMS can be obtained from the circuit: a voltage divider gives a small monitored output for Unit 2.

### Unit 4: High Stability Generators

Two generators are required: one for the drive oscillator and the other for the mixing oscillator. The circuit of each generator is shown in Fig. 8. It is a modified frequency meter: government type BC221. The modification, in the anode of the VT 167 tube, allows the primary oscillator frequency rather than the beat frequency to be amplified, although the beat output is still retained for checking the variable oscillator frequency against the standardizing crystal. It is the short-term stability of this generator that is important. Beating the output against a crystal oscillator showed that the short-term stability at 120 kc/s was of the order 0.03 c/s, and that the drift over long periods was less than 3 c/s. A 10 v change of the H.T. moved the frequency by 3 c/s. These shifts are sufficiently low for the purposes of these experiments. The generators are mounted on flexible supports to reduce frequency shift due to vibration or frame distortion.

### Unit 5: Frequency Dividers

The frequency meters give a signal from 120 to 250 kc/s, and the range to be covered is 1 kc/s to 200 kc/s. Hence frequency division is needed. The circuit is shown in Fig. 9; there is one such circuit for either generator. Two blocking oscillators are used. The first is triggered by the incoming sine wave from the frequency meters and converts the signal to a pulse train of the same frequency. The second is free running and locks into a submultiple of the input. Note that the connection is such that the second blocking oscillator is triggered not by the initial rise of the first but by the ringing return, the first transformer being slightly underdamped. This arrangement was found to be the most stable. Care has to be taken to set the free running frequency fairly close to a submultiple of the master oscillator frequency or irregular triggering will result. The triangular wave output from the grid was found to be most convenient for triggering the following oscillators.

For the lowest frequencies, single stage division is not sufficiently stable. It is necessary to use both dividers in series, suitably increasing the grid resistor on the second divider.





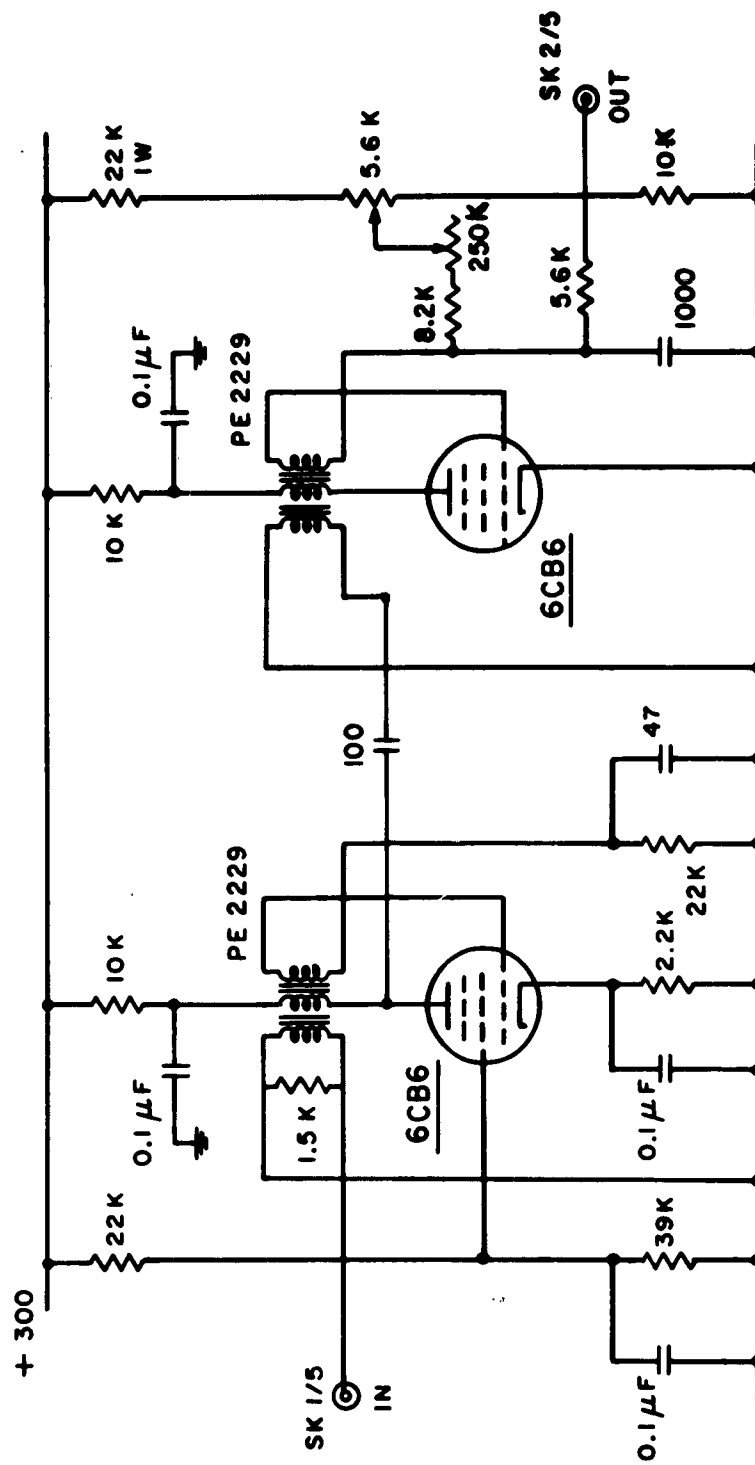


FIG. 9 - FREQUENCY DIVIDER

#### Units 6-7: Locked Oscillators

Hewlett-Packard oscillators Type 200 GR are employed here. One is fed into the mixer circuit, SK 3/2 of unit 2, and the other to the final drive output SK 1/3 of unit 3. The oscillators used a Wein bridge circuit which is not intrinsically very frequency-stable, but which can be readily locked to the output from unit 5 by a 3  $\mu$ F capacitor connected to the grid of the first oscillator tube. Complete locking was obtained for  $\pm 2$  percent changes of dial setting.

#### Unit 8: Recorder

The Bruel and Kjaer Type 2305 logarithmic recorder was found to be most suitable. The maximum writing speed is 1000 db/sec; if one then takes 300 db/sec as being measurable, this limits the maximum log. decrement that can be measured to  $5 \times 10^{-3}$  at 10 kc/s and  $5 \times 10^{-4}$  at 100 kc/s. However, at these relatively high damping values, resonance-width measurements become sufficiently accurate to use, replacing decay-time measurements.

#### Unit 9: Cart Circuits

These circuits consist of AC supplies to the pumps and vacuum gauge, together with a water-pressure actuated switch to protect the furnace and diffusion pump.

#### Unit 10: Detector Circuit

The circuit is shown in Fig. 10. The 36 Mc/s oscillator is loosely coupled to minimize fluctuations in frequency due to the tube, and has a small extra tuning capacitor in addition to that formed by the grid and leads. A cathode follower stage feeds the twin shielded lead to the discriminator-amplifier with a signal of about 1 v amplitude.

#### Unit 11: Furnace Control

This consists of a West Instrument "Gardsman" furnace supply unit, which controls a saturable core reactor. The furnace is fed from these circuits through a step-down transformer: Jefferson type 248-171. Attempts to install automatic control were frustrated by disturbance of the sensing thermocouple by the drive voltage within the furnace. At 1000°C a drift of several degrees occurred on switching on the drive, and this could not be reduced much by shielding arrangements.

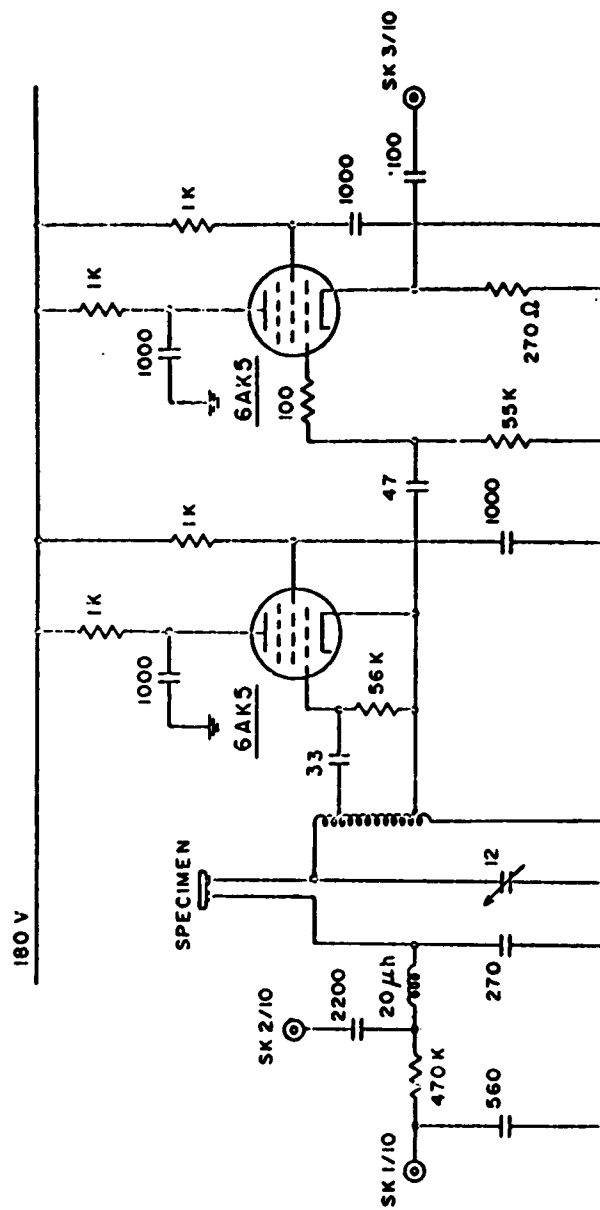


FIG. 10 - DETECTOR CIRCUIT

#### **Unit 12: Vacuum Gauge**

The relatively simple Philips gauge is used here: Veeco type DG-2.

#### **Units 13, 14, 15: Power Unit**

These are standard commercial units giving stabilized supplies of the following values: 250 v, 160 mA; 180 v, 45 mA; 200 v to 800 v, 1 mA; and also 6.3 v heater supplies.

#### **Unit 16: Plug Interchange**

Figure 11 shows this unit. It contains a switch which simultaneously cuts off the drive generator amplifier and the bias supplies, thus removing any interference which might otherwise occur in the recording of the specimen decay-curve. Capacitors can also be switched to slow down the shut-off rate of the bias voltage. This arrangement is needed since for some types of specimen mounting a rapid shut-off was found to produce bouncing of the specimen, with a consequent modulation of the decay curve. A further switch allows monitoring of either the specimen resonance or the frequency divider circuits.

### **OPERATION OF SYSTEM**

To obtain reliable results, it is necessary to reduce the noise to the lowest level and, for the higher values of damping, to have a sufficiently broad pass band. The narrowest band gives the greatest noise reduction, although its use would cause considerable error for logarithmic decrements of greater than, say,  $10^{-4}$  at 100 kc/s. It is also convenient to use broader bands if the specimen temperature drift is at all rapid, since otherwise the consequent change of frequency during decay can produce an effective change of amplifier gain.

Figure 12 shows the overall detector curve: Unit 2 meter reading plotted against gap width as read on the micrometer. At a gap width of 0.1 mm, the sensitivity is 5 microvolts per Angstrom. For a gap utilizing a plate and conducting specimens, the sensitivity is about ten times as great. Determination of absolute vibration amplitudes of a heated specimen is not easy, however, since relative movement of the grid wires can change the capacitance and hence produce an uncertainty in the gap width. It is proposed in the future to install a calibrating system.

It has been found necessary to support the specimen in the manner described, by wires passing through holes, to reduce the extraneous



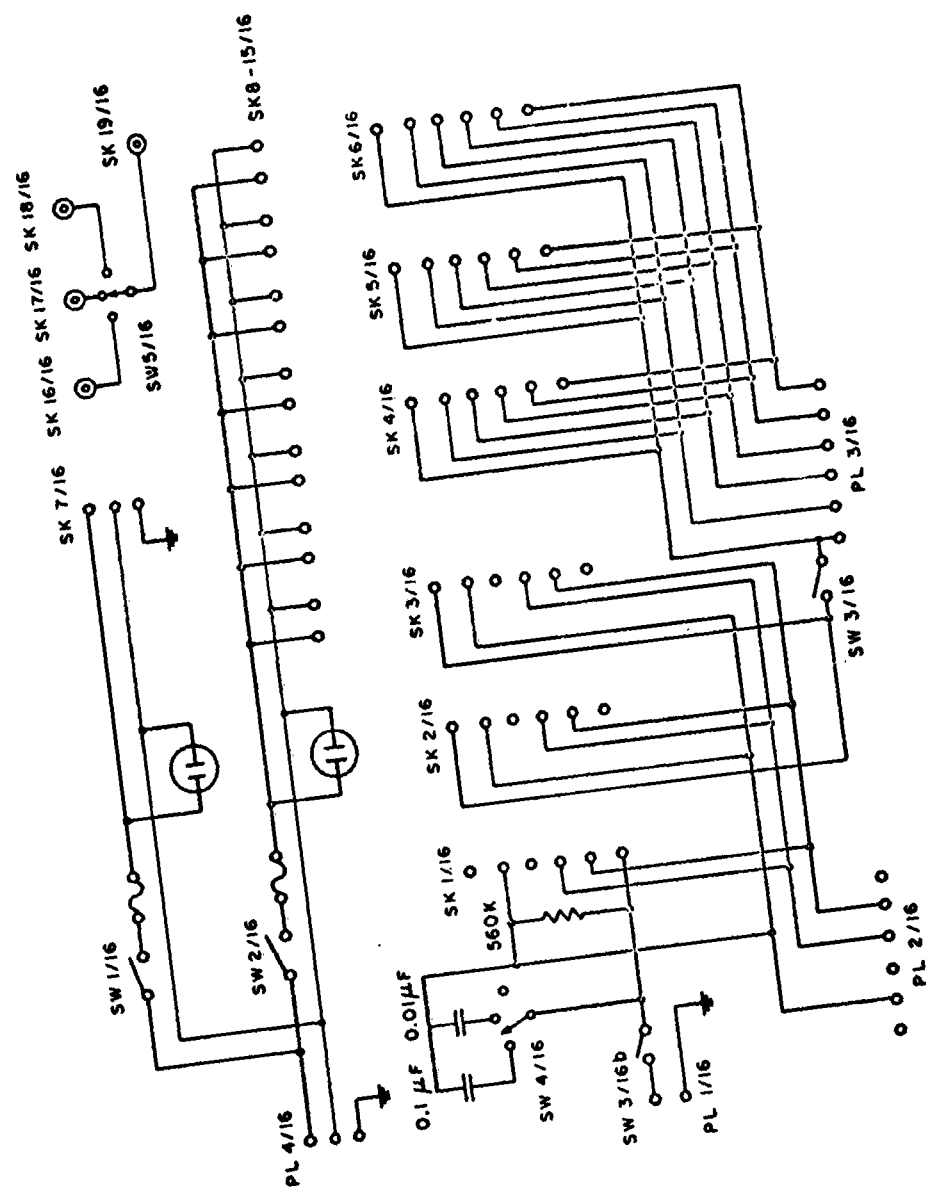
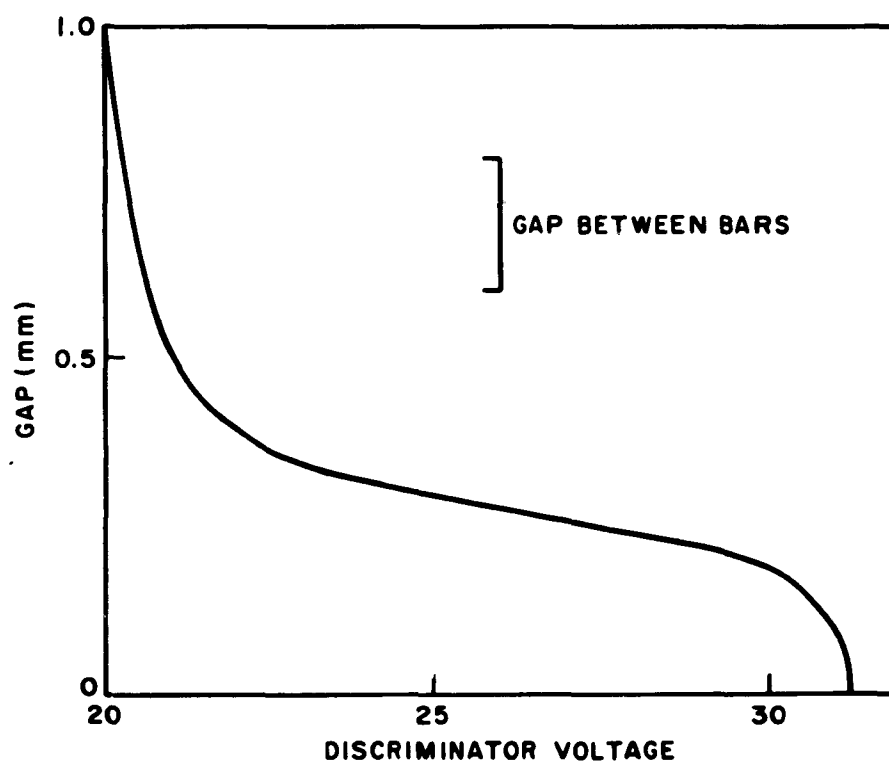


FIG. 11 - PLUG INTERCHANGE



**FIG. 12 - DETECTOR CURVE**

damping to a sufficient low value. Four-wire suspension, with the wires gripping either side, was found to be unsuitable. Even with the present system, occasional high values of damping are attributable to wire friction, probably occurring as the wire slips during heating. The background friction, however, with a specimen 20 x 4 x 2 mm, is about  $10^{-6}$ .

Since a thermocouple cannot be left in contact with the specimen, temperature readings can only be made when the furnace has reached an equilibrium state. At lower temperatures this would prolong the measurements unduly, since about 1 hr. is required for a reliable reading at 300°C. Hence the usual practice is to use the specimen resonance frequency as an index of temperature, taking check-points at the higher temperatures so that any possible anneal may be watched. It turns out that, for the materials studied here, the elastic modulus is sufficiently stable for this temperature measurement method to be reliable.

#### GRID CAPACITANCE CHANGE

An analytic form for the capacitance between the sets of grid wires for arbitrary spacing of the dielectric medium would be exceedingly complicated to compute. The argument that follows gives a value for the sensitivity of the system at a spacing which would represent a reasonable working point.

Smythe<sup>14</sup> gives a formula, derived by a conformal transformation method, for the capacity in the fringing field between two sets of bars of width  $a$  and spacing  $g$ . It is

$$\Delta C = \frac{2n \epsilon_o w}{\pi} \left[ \left(1 + \frac{a}{g}\right) \ln \left(\frac{4g + 3a}{2g + a}\right) - \frac{1}{4} \frac{a}{g} \ln \frac{(4g + 3a)}{(2g + a)^2} \right]$$

where  $\epsilon_o$  is the capacitance of free space  
 $w$  is the breadth of the grid  
 and  $n$  is the number of gaps.

If we now assume that this fringing field is confined to the region above the grid plane, and that insertion of a medium of dielectric constant  $K$  in the region does not change the flux distribution below the plane, then the change in capacitance due to the medium will be

$$\delta C = (K-1) \Delta C$$

If the medium is moved away, it can safely be assumed that at a distance equal to the grid spacing  $g$ , the extra capacity due to the medium will be a fraction  $a$  of  $\delta C$ , which will be of the order of one half. Thus at some point between this spacing and contact,  $dC/dy$  will assume the value  $(1-a) \delta C/g$  and this point will represent a useful working point.

Inserting values of

$$w = 3 \times 10^{-3} \text{ m}$$

$$K = 10$$

$$a = 2 g$$

$$n = 10$$

$$g = 2 \times 10^{-4} \text{ m}$$

we have

$$\left( \frac{dC}{dy} \right) = 10^{-8} \text{ Fm}^{-1}$$

and so

$$\frac{df}{dy} = \frac{1}{2} \frac{f}{C} \frac{dC}{dy} = 1 \text{ cycle per Angstrom unit displacement.}$$

## Section IV

### SPECIMEN PREPARATION

#### FORM OF SPECIMEN

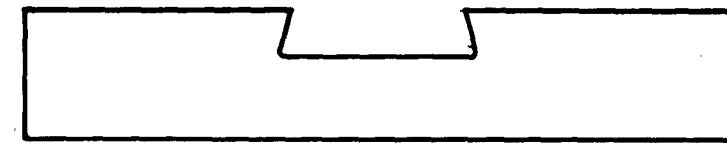
Most measurements have been carried out on bars in the first flexural mode of vibration. The nodal points for this mode lie at 0.224 of the length from either end of the bar. It has been found that unless the support wires lie close to the node, they give rise to excessive losses; hence it is necessary to drill holes at the nodal points and pass the support wires through. Drilling was carried out for all materials using an ultrasonic machine, boron carbide abrasive, and a tungsten wire bit.

Specimens of silicon and silicon carbide were initially cut out with a diamond wheel. The cutting marks were ground away with a fine abrasive and then, at least in the case of silicon, the ground surface etched away. An etch was chosen which left a rough surface, to minimize slipping of the support wires. Care was taken to avoid contamination of the specimen during mounting. The zinc oxide crystals were already in the form of hexagonal prisms and were measured in that form.

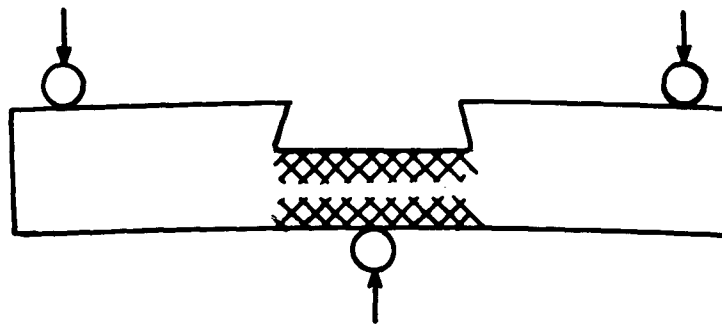
It is convenient to be able to measure a specimen at a number of different frequencies. This can be achieved by cutting a dumbbell form, whose frequency is altered by subsequent thinning of the center section. The shape and sequence of cutting of the specimen is shown in Fig. 13. For a given size of the inertial end-masses, the frequency varies as the  $3/2$  power of the thickness of the center bridge section:

$$f = \frac{1}{2\pi} \sqrt{\left( \frac{E D^3}{L \rho a b (a^2 + b^2)} \right)}$$

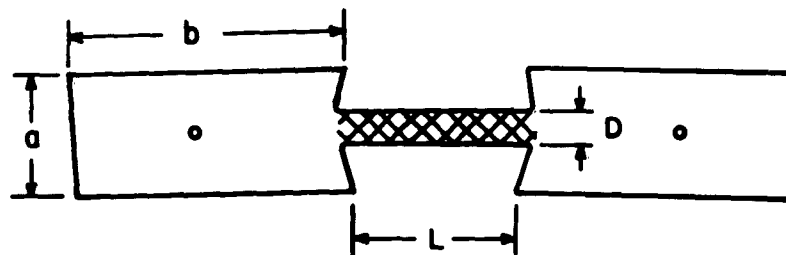
The frequency of a given specimen may be conveniently varied by masking the ends with a cement layer and etching down the center bridge. The procedure for introducing dislocations by bending is designed to approach the ideal of uniform density: the arrangement is such that the second cut forming the bridge removes the neutral axis and hence, on further etching, the dislocation density averaged across the specimen remains approximately constant. It would be more desirable to have a completely homogeneous dislocation distribution across the bridge, such as would be formed by tensional yielding, but further development of the deformation apparatus would be required for this to be achieved.



(a) FIRST CUT



(b) BENDING, SHOWING APPROXIMATE DISTRIBUTION OF SLIP PLANES



(c) SECOND CUT. FURTHER THINNING OF BRIDGE SECTION MAINTAINS AVERAGE DISLOCATION DENSITY.

**FIG. 13 - SEQUENCE OF BENDING AND CUTTING DUMBBELL SPECIMEN**

In analysis of the internal friction results, it is assumed that the measured internal friction is entirely due to the bridge section. Consideration of the elastic energy distribution shows that the ratio of bridge energy: inertial mass energy is

$$\frac{W}{W'} = \left(\frac{a}{D}\right)^3 \frac{L}{2} \frac{3}{b} \quad (4.1)$$

This factor gives the predominance of the contribution from the material of the bridge over that from the inertial masses. During deformation, the inertial masses remain more or less undeformed, and hence their internal friction is relatively low at the higher temperatures, so that the average internal friction is reduced. Equation (4.1) shows that, for the dimensions used in practice ( $a/D > 3.5$ ,  $L/b = 0.6$ ) the error introduced by the assumption of completely rigid inertial masses is less than 2 percent.

The frequency range may be further extended by measuring the internal friction in longitudinal vibration. For dumbbell specimens, the longitudinal frequency will be of the order 10 to 50 times that of the flexural. However, the error due to non-rigidity of the inertial masses will be greater for a given configuration since the energy density varies only as the inverse square of the thickness. Hence a ratio  $D:a$  of less than 1:7 is required for an error of less than 2 percent.

The small size of the available crystals precluded the use of dumbbell specimens for silicon carbide or zinc oxide.

#### ORIGIN AND NATURE OF MATERIAL

The silicon was obtained from the Semi-Elements Corporation. It was 100  $\mu$ -cm material, having a very low oxygen content (with the exception of one specimen which has been deformed but whose internal friction characteristics have not yet been studied). Specimens were cut with axes in either  $[111]$  or  $[100]$ .

Although high purity silicon carbide crystals can be grown by vapor deposition in the laboratory, none have been acquired which were large enough to measure. The material reported on here was taken from the relatively large crystals which grow around the blow-holes in a commercial furnace: it was supplied by Norton Abrasive Corporation. Table I gives a spectrochemical analysis of impurity content. In appearance it was pale green, slightly streaky. An x-ray analysis of the polytype has not yet been carried out, although it is probably the most common one found under these circumstances, type 6H. The specimen axis was  $[1120]$ .

The zinc oxide crystals were kindly donated by the 3M Company Research Laboratories. They were grown by Dr. F. Ham of the laboratories by vapor deposition under carefully controlled conditions. The crystals were apparently quite clear and colorless, and of very regular form. The axis was [0001].

Table 1

ANALYSIS OF CHIEF IMPURITIES IN SiC SPECIMEN 310  
(WEIGHT PERCENTAGES)

	Ag	Al	Ba	Ca	Cr	Cu	Fe	Mg	Mo	Ti
Spectro- graphic: Approx.	0.03	0.1	0.003	0.03	0.01	0.001	0.01	0.03	0.01	0.03
Chemical Analysis		0.099								



## Section V

### DEFORMATION OF SILICON

#### APPARATUS

Silicon becomes plastic above 800°C, deformation often occurring after the lapse of a noticeable incubation time. Ideally, deformation should be performed in a vacuum to minimize contamination, but the elaboration of the apparatus required to operate in vacuum is not justified, since there is no apparent contamination when a non-oxidizing atmosphere is used. The simplest method of deformation, that of bending, is employed. Strain vs. time curves are recorded during deformation.

The apparatus is shown in Fig. 14 and in section in Fig. 15. The specimen is loosely held between two stainless steel chucks equipped with sapphire jaws, supported on stainless steel cross-wires. A central stainless steel push-rod, also with a sapphire tip, is used to apply a three-point bending stress to the specimen. A cranked lever at the far end of the push-rod couples it to a hanging weight, the object of this system being to apply a constant force. When large angles of bend are produced, a similar push-rod system on the opposite side of the sample can be used to straighten the specimen. The specimen, push-rods, and chucks are enclosed in a silica tube, through which a stream of 90 percent nitrogen: 10 percent hydrogen passes. The whole is heated by a surrounding resistance furnace.

Two coaxial stainless steel tubes are used to transmit the deformation data to a convenient location outside the furnace. The inner tube is fastened to the chuck assembly, while the outer tube is coupled to the rod that applies the deformation stress. Measurement of the relative motion of these two coaxial tubes then allows determination of the sample deformation, without introducing errors due to differential thermal expansion of spatially separated members, or to stresses in the rods.

The relative motion of the two tubes, and hence the deformation of the sample, is measured as follows: a light metallic ring, fastened at diametrically opposite points to each of the two tubes, flexes when relative motion of the tubes occurs. Strain gauges fastened to the ring sense the magnitude of this flexure. If we assume that the ring deformation is small, and that the deformed ring is elliptic, then the maximum deformation of the ring occurs along an axis perpendicular to the axis containing the tubes. The relative change in curvature along the two axes will be equal in magnitude so that

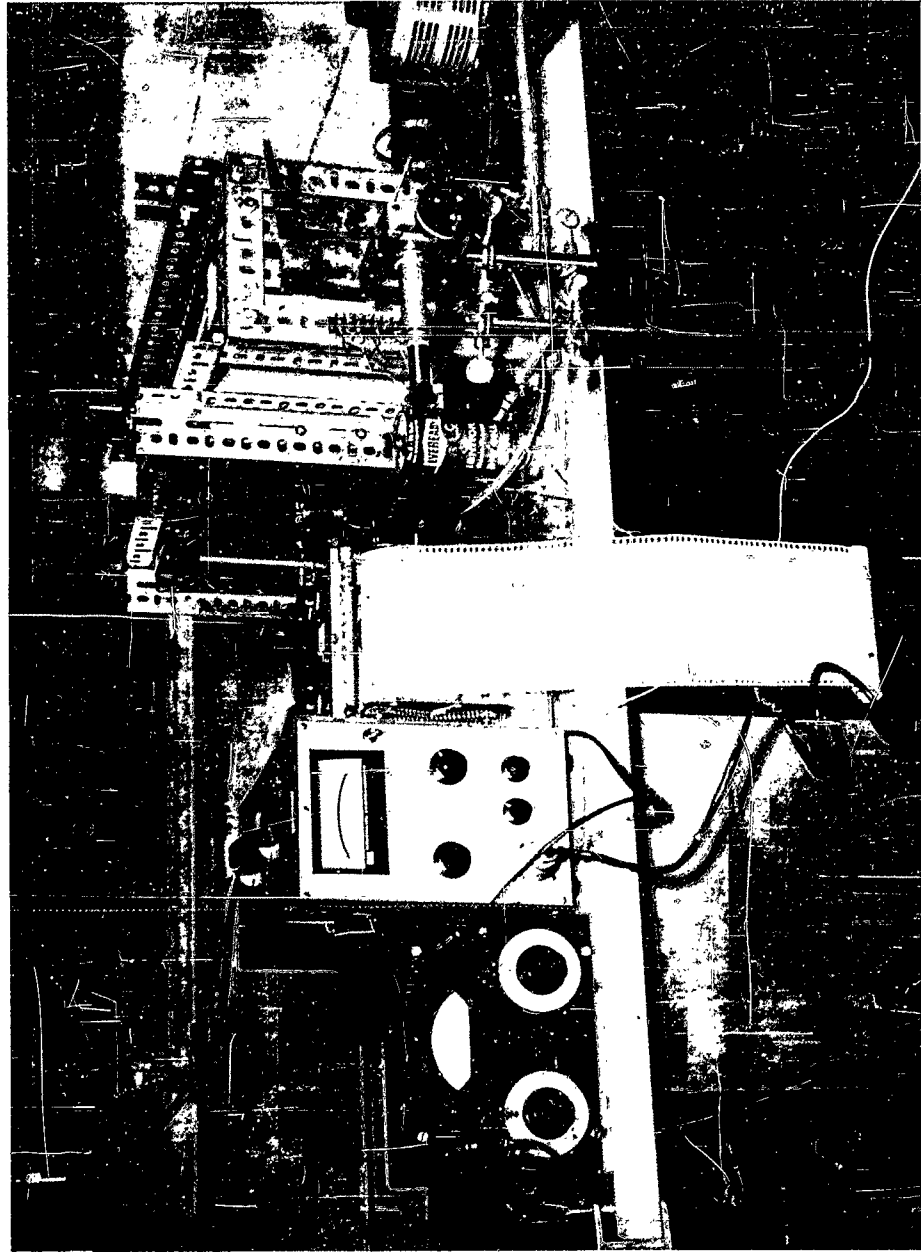
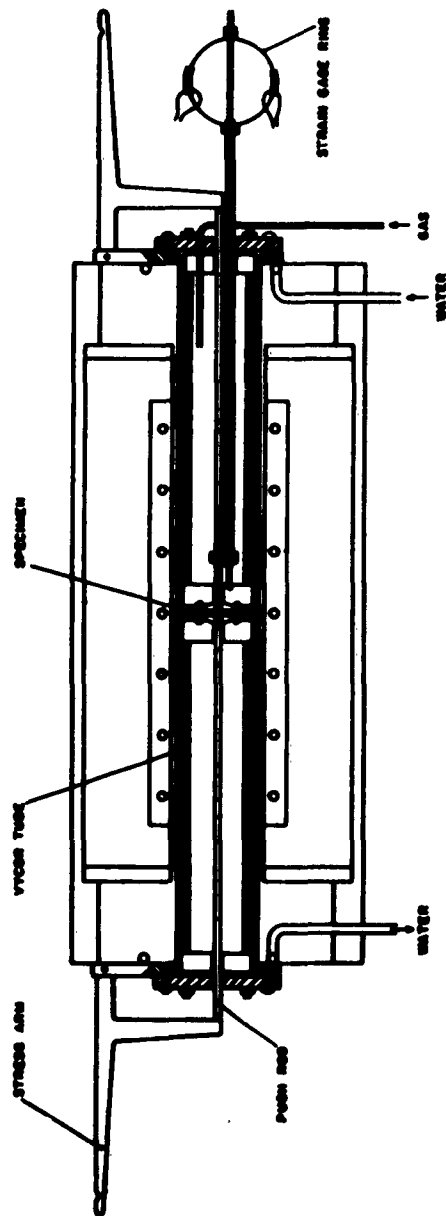


Fig. 14 - PHOTOGRAPH OF BENDING APPARATUS



**FIG. 15 - DIAGRAM OF BENDING APPARATUS**

$$\frac{\delta A}{A_0} = \frac{\delta B}{B_0}$$

where  $A_0$  and  $B_0$  are the semi-major and semi-minor axes. Strain gauges are mounted on the ring at the maximum flexure points, (two outside, two inside), connected in a bridge-circuit arrangement. For a ring of diameter  $D$ , thickness  $t$ , the gauge factor  $G$  of the strain-gauges being defined as

$$G = \frac{\delta R/R}{\delta L/L}$$

and where the supply voltage is  $V$ , the ratio of sample deformation  $\delta S$  to output voltage  $\delta E$  is

$$\frac{\delta E}{\delta S} = \frac{3VGt}{D^2}$$

(Here we have assumed that the four strain gauges have the same zero-strain resistance.)

In the present circuit a ten turn potentiometer has been inserted in the bridge to obtain balance conditions. The gauge resistance is  $120\Omega$ , and the potentiometer is shunted by  $0.2\Omega$  which gives a conveniently fine adjustment while allowing unbalance due to initial strain in the gauges to be corrected. In this experiment

$$D = 53 \text{ mm}$$

$$t = 0.6 \text{ mm}$$

$$G = 2$$

$$V = \text{volts}$$

The calculation gives

$$\frac{\delta E}{\delta S} = 3.8 \text{ mV/mm}$$

whereas the measured value is

$$\frac{\delta E}{\delta S} = 4.2 \text{ mV/mm}$$

The electrical measuring apparatus consists of a Keithley 150A Microvoltammeter, and a Varian Recorder. The noise level corresponds to a deflection of one micron. Long-term stability is sufficient to allow accurate recording of the deformation-time curve over periods of the order of ten minutes.

#### CREEP CURVES

A number of specimens have been deformed at 950°C. Figure 16 summarizes the creep data for these specimens, while Table 2 gives information on the total bend size orientation, and purity. The bend force is that actually applied to the push-rod, and the thickness is that during bending. The bend angle was measured optically, by reflecting a projected spot of light off the faces of the crystal. In some cases, creep occurred in several stages, as extra weights were added. The zeros of time and beam deflection are taken for each stage as being the state when the extra weight was added. Specimens 2042 onward were polished in CP-4 etch\* before bending. In the case of 2033 the bromine was omitted from the etch, while for 2031 and 2034 a non-polishing HF+HNO<sub>3</sub> etch was used.

The curves of Fig. 16 are not very consistent, and it is not possible to draw any exact conclusions. The difference between deformation curves 2042 and 2044 is most noticeable, since these specimens were nominally deformed under identical conditions. Only 2042 shows an incubation time. There is a general tendency for specimens having the largest mean tensile stress (last column of Table 2) to deform the most rapidly, but since many of the curves are for already worked specimens, the relationship between stress and creep rate cannot be readily deduced. The oxygen content of 2053 may be inhibiting creep

---

\* Glacial acetic acid: 70 percent HNO<sub>3</sub>, 49 percent HF in proportions 3:5:3, plus 5 cc Br per liter.

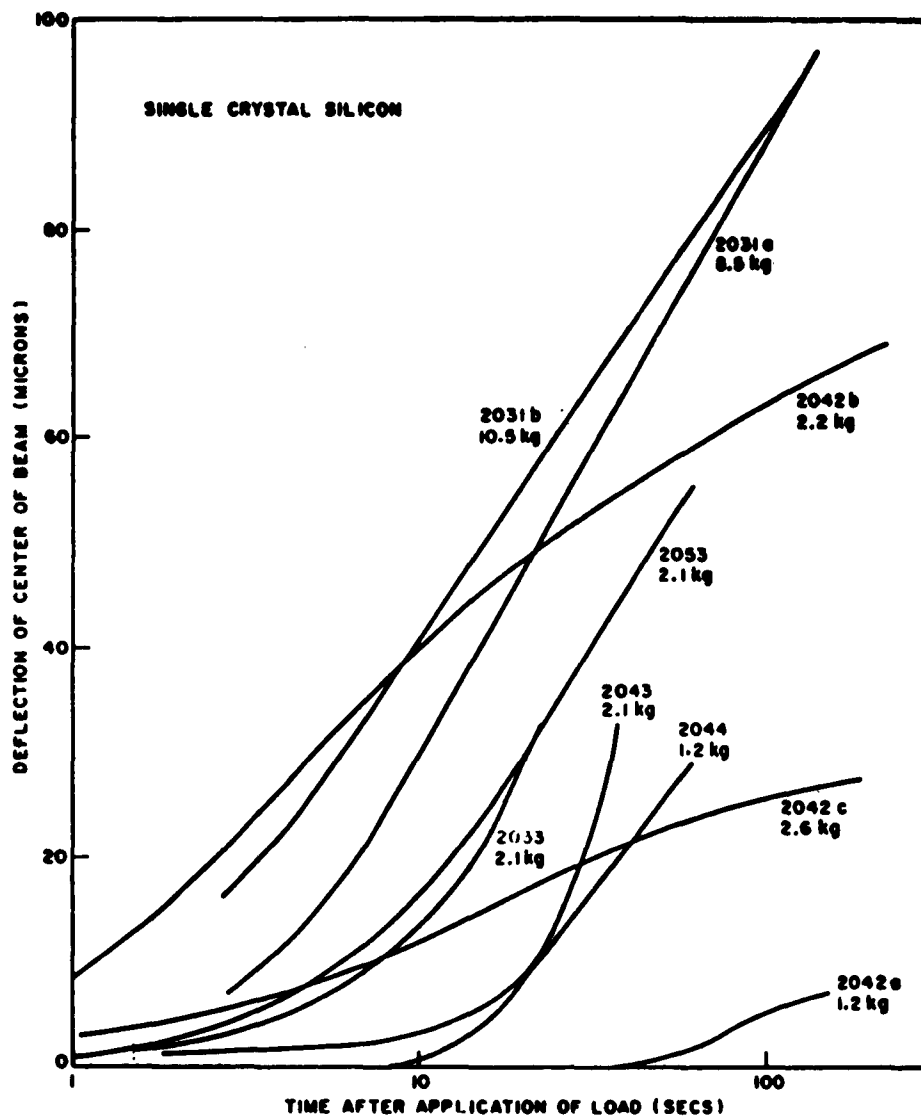


**FIG. 16 - CREEP CURVES OF SILICON SPECIMENS**

Table 2  
DATA ON DEFORMED SPECIMENS

Specimen Orientation	Oxygen conc. (cm <sup>-3</sup> )	Thickness (mm)	Total Bend (degrees)	Bend Force (kg)	Mean tensile stress dyne cm <sup>-2</sup> x 10 <sup>-8</sup>	
2031	111	< 10 <sup>16</sup>	2.4	4.7*	8.5-10.5	6.4-8
2033	111	"	1.65	0.52	2.1	3.5
2034	111	"	2.4	0.55	2.1	1.6
2042	100	"	2.25	1.68	1.2-2.2-2.6	1.4-2.6-3.1
2043	100	"	2.35	0.48	2.1	1.7
2044	100	"	2.15	0.39	1.2	1.6
2053	100	10 <sup>18</sup>	2.25	0.86	2.1	2.5

\* straightened

to some extent, but this is not a strong effect. With the exception of 2033 and 2043, which had the lowest stress applied, the curves tend to show a region of logarithmic creep, an approximately straight line on the strain vs.  $\ln t$  plot, followed by a flattening off, presumably due to work-hardening. Paradoxically, the two specimens having the most rapidly increasing creep rate had almost the lowest applied average stresses. These two have differing orientations, showing that this is not a dominant factor. The data of Penning and de Wind<sup>15</sup> in germanium show similarly shaped curves to these in silicon. However, work-hardening seems to occur more readily in silicon, since strain magnitudes which give rise to work-hardening in silicon lie in the region of maximum creep rate in germanium. Direct comparison of the two sets of measurements is not possible, due to the difference in temperature of deformation (0.56 of the melting point in germanium, 0.72 in silicon).

It is evident that to resolve the situation more clearly, measurements are required on many more specimens, with close attention to surface conditions probably being necessary. Such a study is beyond the scope of this work.

## DISLOCATION DISTRIBUTION

Dislocation distributions after plastic deformation have been studied using the etch-pit method. After an initial polish in CP-4, the iodine etch\* described by Queisser<sup>16</sup> was employed. Pits appear after a few seconds with this etch and are very marked after about one minute. Figures 17, 18 and 19 show patterns developed on the sides of three of the specimens of Fig. 16, the magnification being the same in all instances. There is a considerable difference between the patterns of 2033 and the other two, dislocations for 2033 being mainly confined to the area shown in the photograph, whereas for 2043 and 2044 the dislocation density remains almost uniform for a central length of about 5 mm along the specimen. The further side of 2033 had a distribution rather more like that of the other two.

The reason for the difference of slip mode probably lies in the different slip plane orientations of the two specimens. Silicon slips on (111) planes; dislocations are in [110] directions and have their Burgers vectors in [110] directions, at least during the initial stages of slip. Thus, for stress in [111], there are three active slip planes; for [110], two, and for [100], four. In each of these cases the resolved shear stress will be a different fraction of the applied stress, due to the different angle the stress direction makes with the plane. A further resolution of the stress occurs in the plane, where a factor of  $\sqrt{3}/2$  is involved for each orientation.

If one considers a bar in three-point bending, the portion near the center experiences both flexural and shear stresses. We now show that the forces on dislocations which produce pure shear can be comparable with those that produce extension or compression in the upper or lower portions of the bar. The stresses on a bar of thickness  $d$  with the two extreme bending points  $L$  apart, and a force  $F$  per unit width applied the center, are as follows:

$$\text{Shear stress } \sigma_s = F/d$$

$$\text{Average tensional stress} = \frac{3 FL}{4 d^2}$$

If now the resolution factors are taken into account, we find that the ratio of shear stress on the plane perpendicular to the bar axis, to the resolved shear stresses on the other three planes is given by

---

\* Glacial acetic acid: 70 percent  $\text{HNO}_3$ : 49 percent HF in proportions 5:4:1, plus 8 gm iodine per liter.



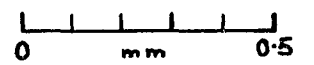
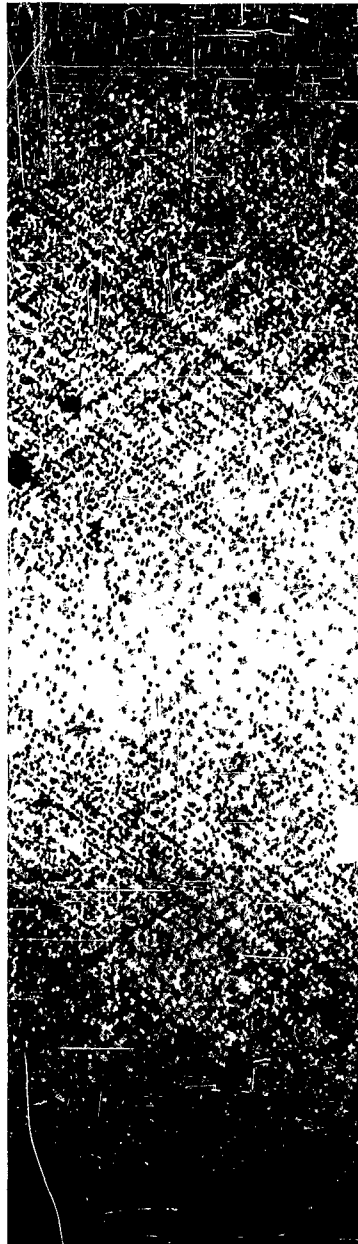
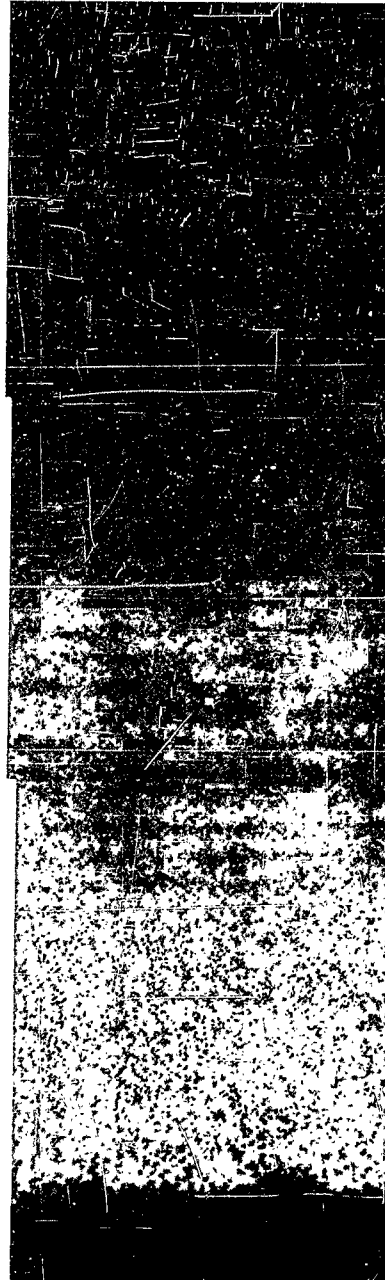


Fig. 17 - DISLOCATION PATTERN IN SILICON 2043



Fig. 18 - DISLOCATION PATTERN IN SILICON 2033



0 mm 0.2

Fig. 19 - DISLOCATION PATTERN IN SILICON 2044

$$\sigma_s / \sigma_s' = \frac{F}{d} \left/ \frac{3F}{4d^2} \right. \cos \theta \sin \theta \cos \varphi$$

where  $\theta$  is the angle between the (111) plane and the bar axis, and  $\varphi$  the angle between the resolved shear stress and the Burgers vectors. For a bar having [111] axis, the ratio becomes

$$\sigma_s / \sigma_s' = 4.9 d/L$$

Thus, a predominant slip on the (111) planes perpendicular to the bar axis, as seen in Fig. 18, would not be expected for an  $L/d$  ratio much greater than 4.9. However, examination of the specimen shows that in fact, due to some form of misalignment, pressure was applied to only about one third of the face. Thus, the shear stress in this region will be increased, whereas the bending stress is almost unaffected, and it is then likely that slip could be preferentially initiated on the perpendicular (111) planes for the specimen which in fact had an  $L/d$  ratio of 10. Even so, special surface nucleation effects may well be involved.

Plots of etch pit density vs. distance from the center of the bar is shown in Figs. 20 and 21. The counts were made from Figs. 17 and 18 and the scatter in values reflects the tendency of the dislocations to lie in slip planes rather than perfectly uniformly. According to the simplest picture of bending, a constant dislocation density should result from a uniform bend. Any dislocation density in excess of this number will be formed of equal numbers of dislocations of opposite sign. It is assumed that this is the case, although there is no way of checking the sign of the dislocations from the appearance of the etch pits. A theory which would account for the distribution shown in Figs. 20 and 21 can be constructed on the assumption of restricted dislocation motion, in the following manner. Let dislocations be generated in the interior of the specimen during slip, and let them move an average distance  $s$  before being stopped. If the dislocations are linear and extend right across the specimen, the strain at any point is given by

$$\epsilon = bs N \cos \theta \sin \theta$$

the resolution factor being required as before. In uniform bending, this strain will also be equal to  $x/R$ ,  $x$  being the distance from the neutral axis; hence

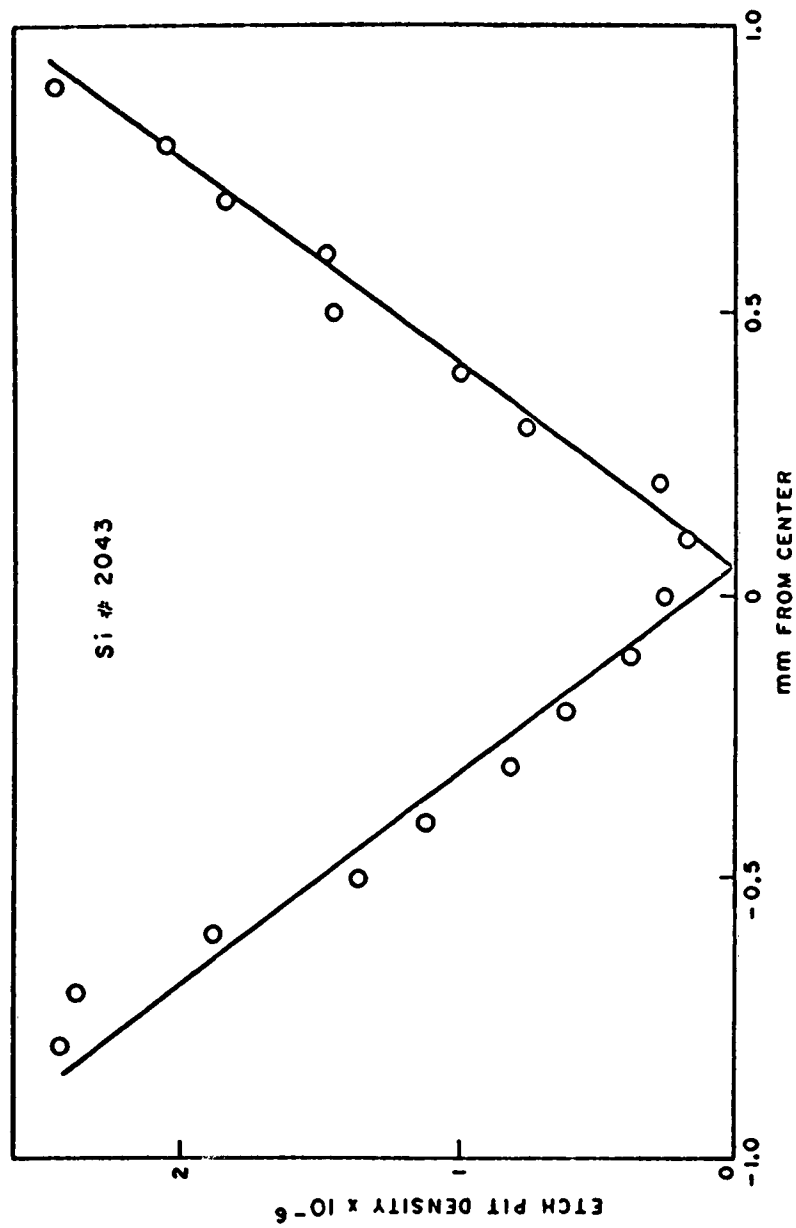


FIG. 20 - ETCH PIT DISTRIBUTION IN 2043

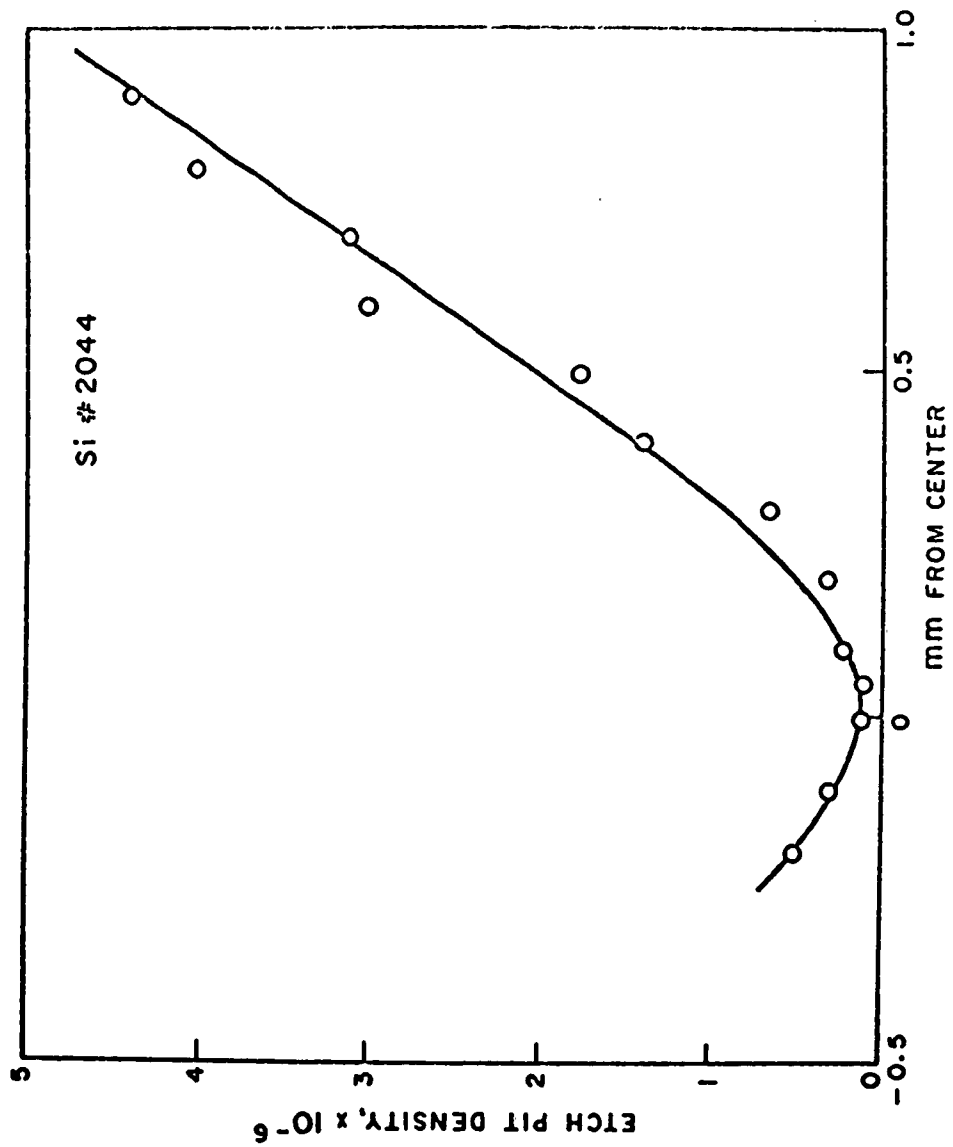


FIG. 21 - ETCH PIT DISTRIBUTION IN 2044

$$s = \frac{x}{Rb N \cos \theta \sin \theta}$$

The slopes  $N/x$  of the straight-line portions of Figs. 20 and 21 are  $2.6 \times 10^8$  and  $6 \times 10^7 \text{ cm}^{-3}$  respectively, while the radii of bend  $R$  are estimated as 70 cm and 60 cm. Hence the  $s$  values for the two specimens 2043 and 2044 are  $2.6 \times 10^{-3}$  and  $1.3 \times 10^{-2} \text{ cm}$ , a small fraction of the total specimen width. The difference between the two values indicates that  $s$  may reduce fairly rapidly with increasing dislocation density.

After vacuum anneal of the specimens, it was found more difficult to develop etch pits, as an irregular background appeared simultaneously with the pits. The reason for this difficulty is not clear, since ideally no change should have occurred in the bulk of the specimen. Satisfactory patterns could be observed, however, in the initial stages while the pits were still very small. Such observations as were made indicated no substantial change in the general dislocation arrangement, during the measurements to be described in the next section, although a precise one-to-one check on the dislocations was not possible.

## Section VI

### INTERNAL FRICTION OF SILICON

#### EXPERIMENTAL RESULTS

In all the plastically deformed crystals which have been measured a steady rise of internal friction has been seen above about 500°C. Figures 22 to 27 show this rise in five different specimens. The frequency of 2042 was varied by thinning the center section of the dumbbell by etching in CP4. Figure 28 shows the internal friction of a specimen which has been heated in the deformation apparatus but not deformed; no high temperature rise is seen, showing that it is solely dependent on the introduction of dislocations into the specimen.

The internal friction curves may be analyzed by subtracting from the total a constant background damping and an electronic damping.<sup>5</sup> The background is due to radiation along the wires, and at lower temperatures is usually the only source of loss. It is assumed temperature independent. The electronic damping may be calculated if the specimen is sufficiently uncontaminated so that the charge carrier lifetime does not drop far below the period of oscillation. When these two losses are subtracted, the remaining curves are very close to the Arrhenius form  $\Delta_d = \Delta_\infty \exp(-H/kT)$ . A small deviation seems to occur at the lower temperatures, while the lowest frequency curve of 2042 shows a leveling-off at the high temperature end. Table 3 gives an analysis of the straight-line part of the dislocation damping curves, together with the mean dislocation densities as given by etch-pit counts, and angle of deformation from optical measurements. The constancy of activation energy for all specimens, independent of deformation angle or dislocation density, is notable, and indicates that a single activated process is involved, rather than a complex of processes. The average is 1.61 eV, with an estimated error of +0.02 eV. The last column of Table 3 gives values of  $\Delta f/N$ ; within the uncertainties of the uniformity of  $N$ , these values may be regarded as approximately constant.

Annealing of the internal friction to lower values is observed in each case. The pattern, however, is not simple. The kink in the heating curve of Figs. 24 and 25 shows an initial limited anneal takes place near 920°C, close to the temperature at which the specimen was bent. The data of Table 3 refers to measurements after this initial anneal. Such an anneal might be anticipated, since the process of deformation is followed by an immediate cooling, and any locally stressed portions of the material which did not anneal out in about 5 minutes would be frozen in. Further stages of anneal are represented by the lower lines in Figs. 22 and 23, the lowest two being measured after 10 minutes at 1040° and then after a further 15 minutes between 1000° and 1040°. No opinion can be given at this stage as to the nature of the annealing process.



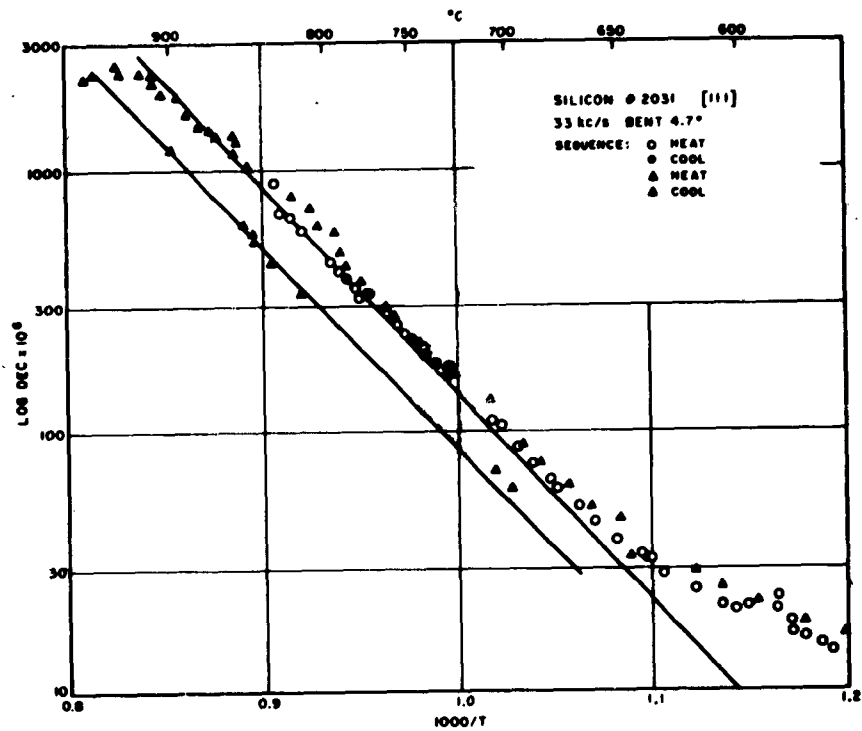


FIG. 22 - INTERNAL FRICTION OF SILICON 2031

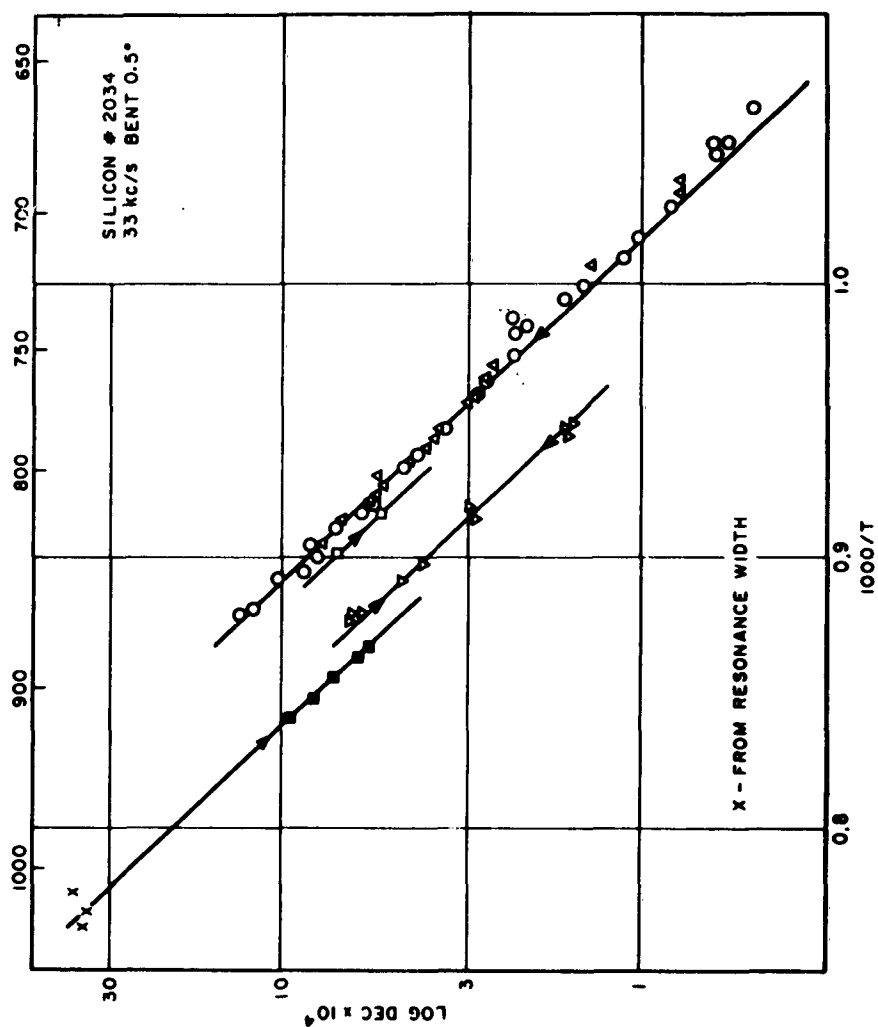


FIG. 23 - INTERNAL FRICTION OF SILICON 2034

Sequence of heating:  $\Delta$   $\circ$   $\square$   $\nabla$   $\times$

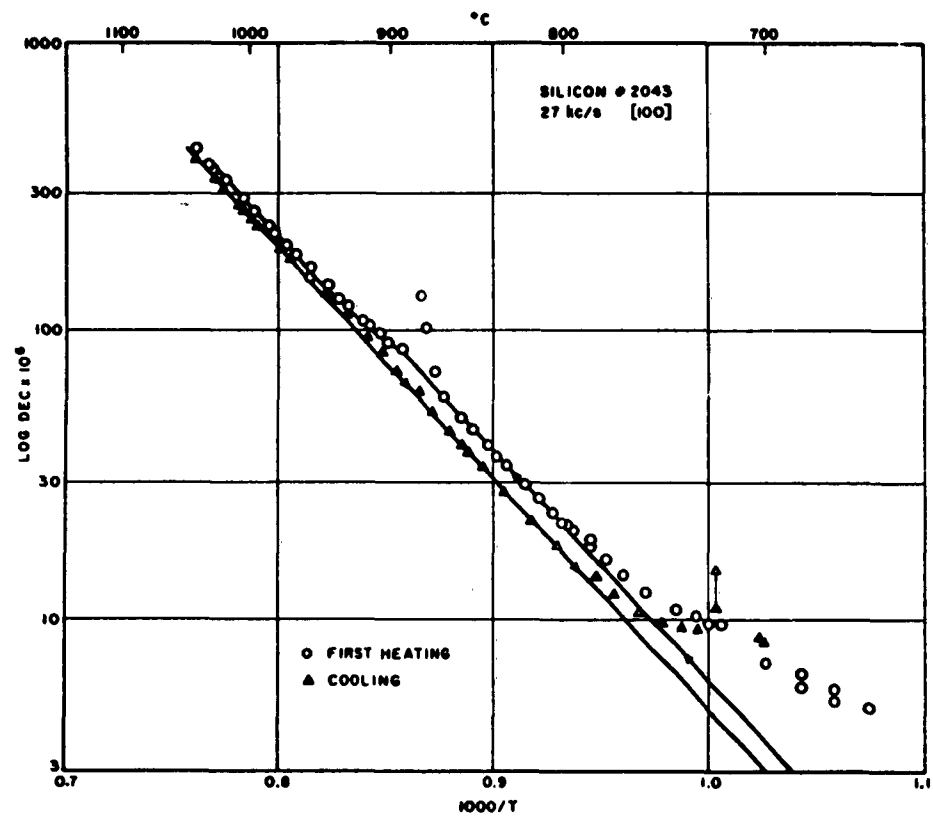


FIG. 24 - INTERNAL FRICTION OF SILICON 2043

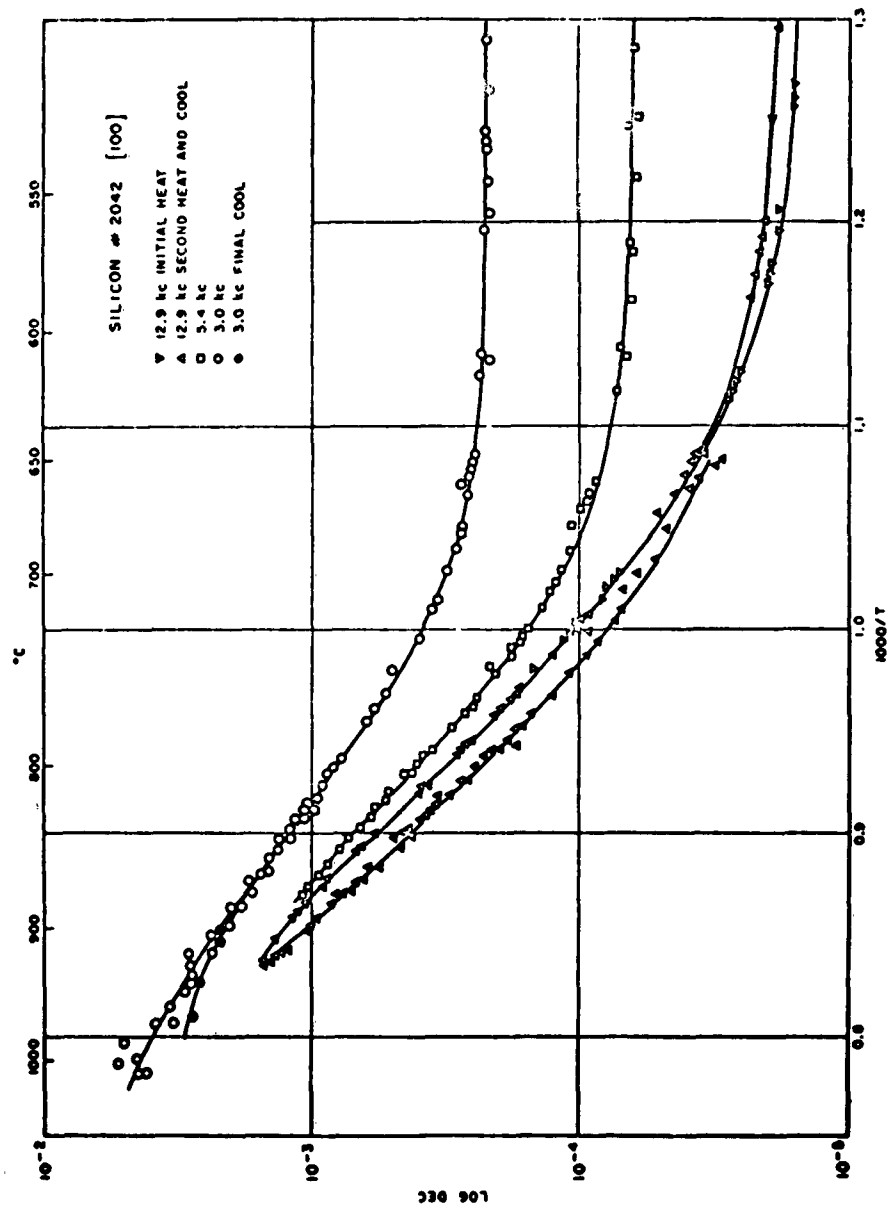


FIG. 25 - INTERNAL FRICTION OF SILICON 2042

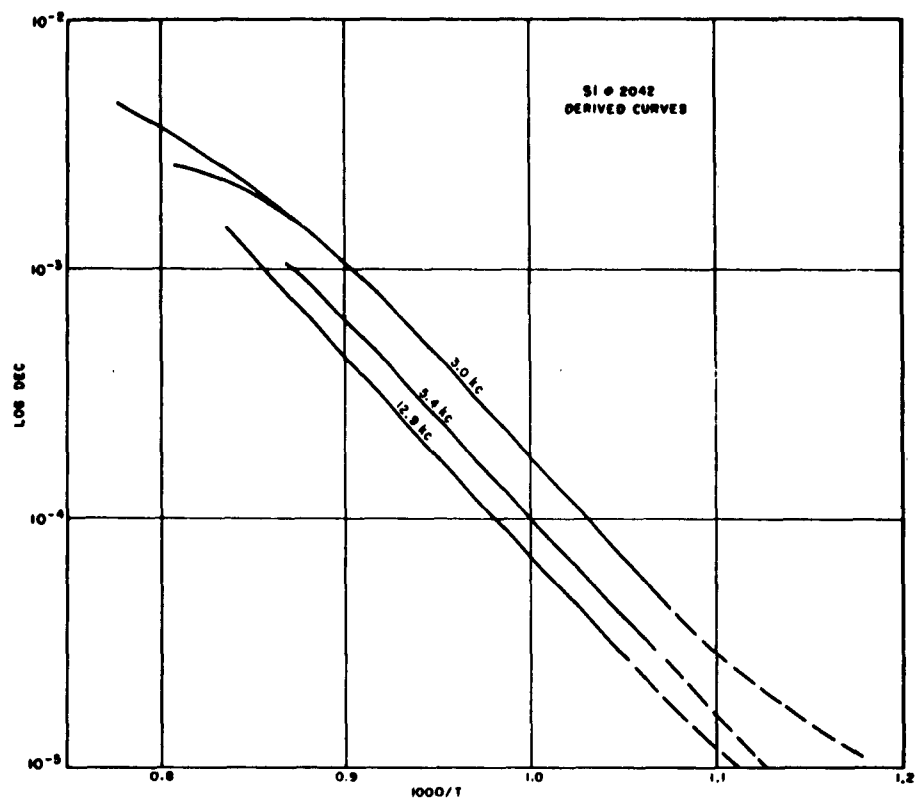


FIG. 26 - INTERNAL FRICTION OF SILICON 2042:  
DERIVED DISLOCATION DAMPING CURVES

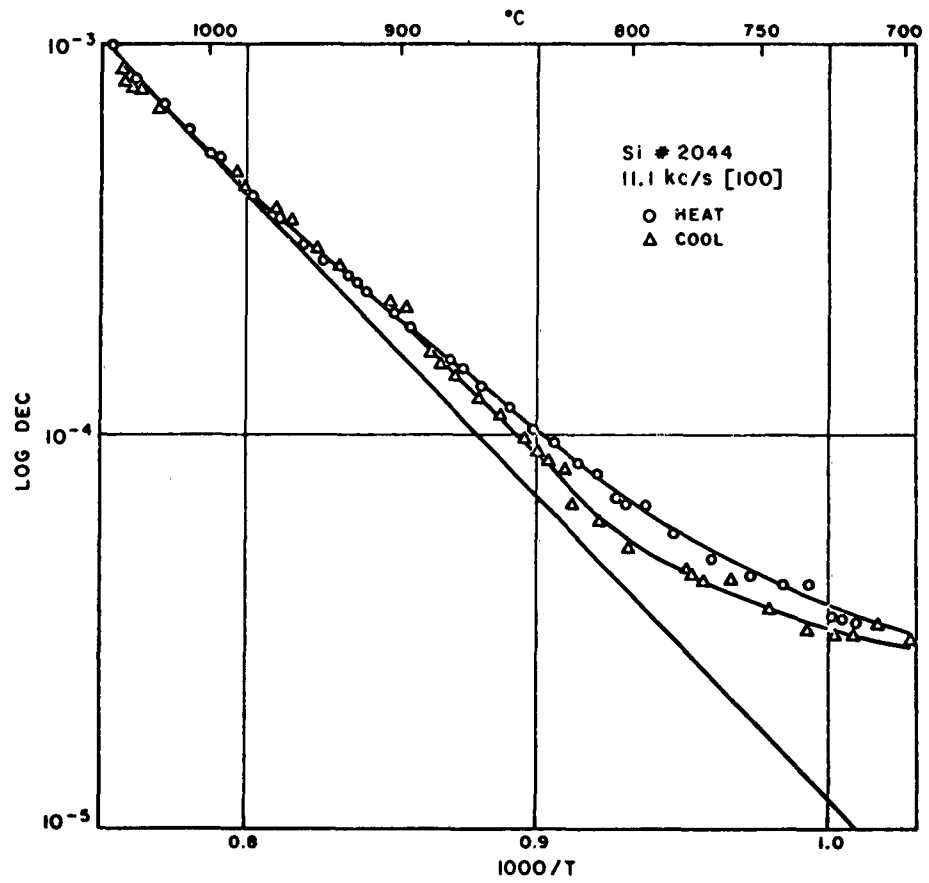


FIG. 27 - INTERNAL FRICTION OF SILICON 2044

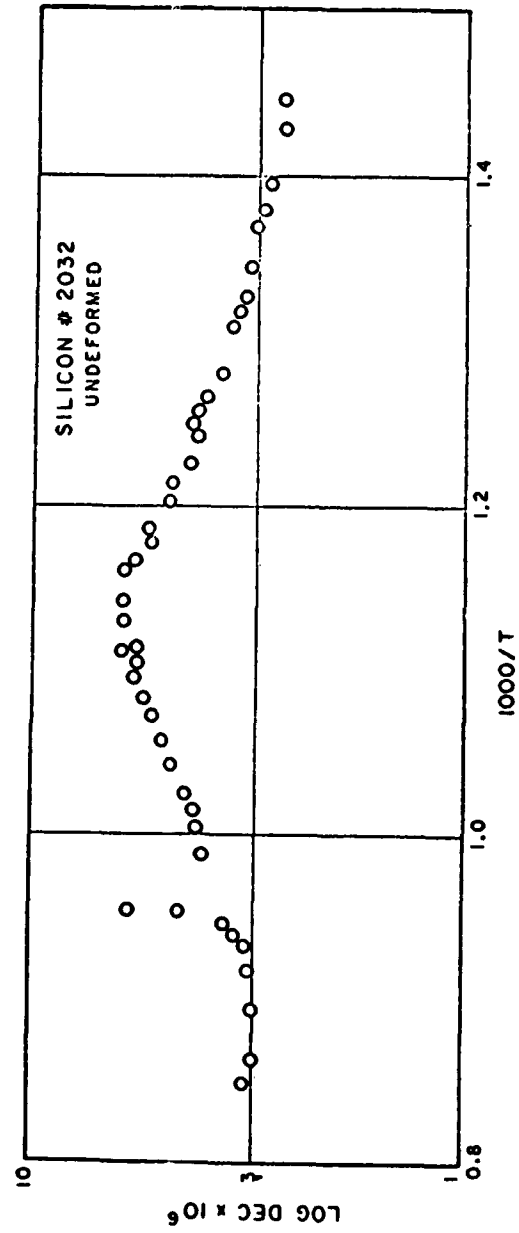


FIG. 28 - INTERNAL FRICTION OF SILICON 2032

Table 3  
DISLOCATION DAMPING IN SILICON

Specimen	Orientation	$\Delta_d \times 10^6$ (1000/T = 1.0)	H (eV)	f (kc/s)	$N_{(av)} (cm^{-2})$	Deformation Angle	$K = \frac{\Delta(1.0) f}{N}$
2031	111	140	1.59	32.2		4.7°	
2033	111	10*		21.8	1 to 9 x 10 <sup>6</sup>	0.5°	21 to 2.4 x 10 <sup>-8</sup>
2034	111	135	1.59	32.6		0.55°	
2042	100	$\left\{ \begin{array}{l} 11.5 \\ 68 \\ 92 \\ 170 \end{array} \right\}$	1.61	65	$\left\{ \begin{array}{l} \\ 1.2 \times 10^7 \\ \\ \end{array} \right\}$	$\left\{ \begin{array}{l} \\ 1.68^\circ \\ \\ \end{array} \right\}$	$\left\{ \begin{array}{l} 5.9 \times 10^{-8} \\ 7.2 \times 10^{-8} \\ 4.2 \times 10^{-8} \\ 4.3 \times 10^{-8} \end{array} \right\}$
			1.61	12.9			
			1.61	5.4			
			1.61	3.0			
2043	100	4.8	1.60	26.4	1.6 x 10 <sup>6</sup>	0.48°	7.9 x 10 <sup>-8</sup>
2044	100	11	1.6	11.1	1.8 x 10 <sup>6</sup>	0.39°	6.2 x 10 <sup>-8</sup>
* non-linear							



A more marked thermal modification of the internal friction occurred in 2033, is shown in Fig. 29. Figure 30 illustrates more clearly the hysteretic nature of the thermal cycling. This specimen showed a rapidly increasing amplitude dependence of internal friction with temperature, and also an increased magnitude, which was retained to some extent on cooling. Behavior of this type suggests that dislocations are being released on heating and taking up loosely pinned positions, from which they slowly diffuse to more firmly pinned positions. The loosely pinned dislocations may then give rise to amplitude dependent damping of the type mentioned in Section II. On cooling, the freed dislocations may well take longer to become locked, but no further dislocations would be freed from their initial positions. Such a model requires further substantiation; as was pointed out, there is no supporting evidence of such motion from the etch pit observations. The unusual mode of slip of this specimen has already been discussed in Section V, part 3. If indeed most dislocations have slipped on the (111) plane perpendicular to the specimen axis, these dislocations will not contribute to the internal friction, and the overall internal friction will be low. The internal friction observations will then refer to dislocations which do not lie in the main slip system.

#### APPLICABILITY OF SDP AND BRAILSFORD THEORIES

Two detailed theories have been proposed to explain dislocation relaxation, both of which depend on kink motion. That of Seeger, Donth and Pfaff<sup>7</sup> assumes that kinks are free to move along a dislocation, once formed, and are only affected by elastic strain fields of other kinks, whereas that of Brailsford<sup>8</sup> assumes a core interaction of the kinks with the lattice, so that kink motion is thermally activated. The SDP theory is based on a string-type model for the dislocation, and hence is consistent with the Koehler-Granato-Lucke theory.<sup>9, 10</sup> Reasons are given in Appendix V for regarding Brailsford's theory as consistent with the KGL theory. Both theories agree with the present experimental results in predicting a constancy of the parameter  $\Delta f/N$ .

In the following discussion these symbols are most commonly used:

G	shear modulus
a	lattice plane spacing
b	Burger's vector of dislocation
T	temperature
f	frequency of mechanical oscillation
$\Delta$	logarithmic decrement.

Interpretation of the graphs given in the SDP paper shows that, according to this theory, the dislocation relaxation frequency is

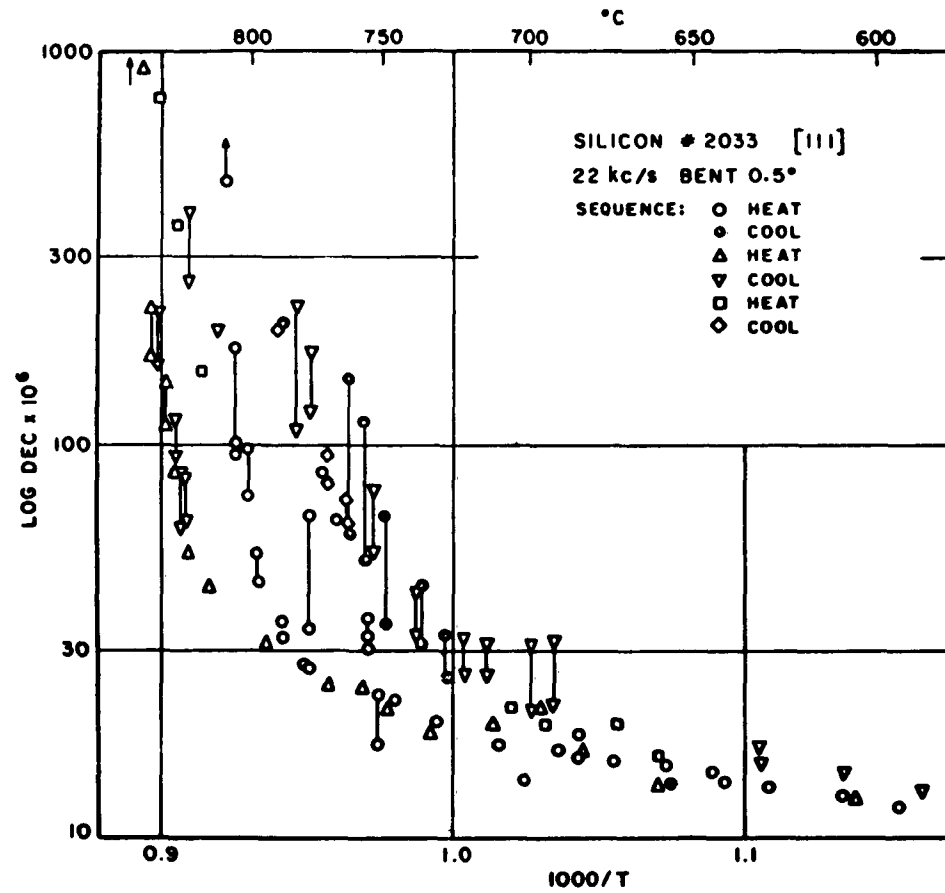


FIG. 29 - INTERNAL FRICTION OF SILICON 2033

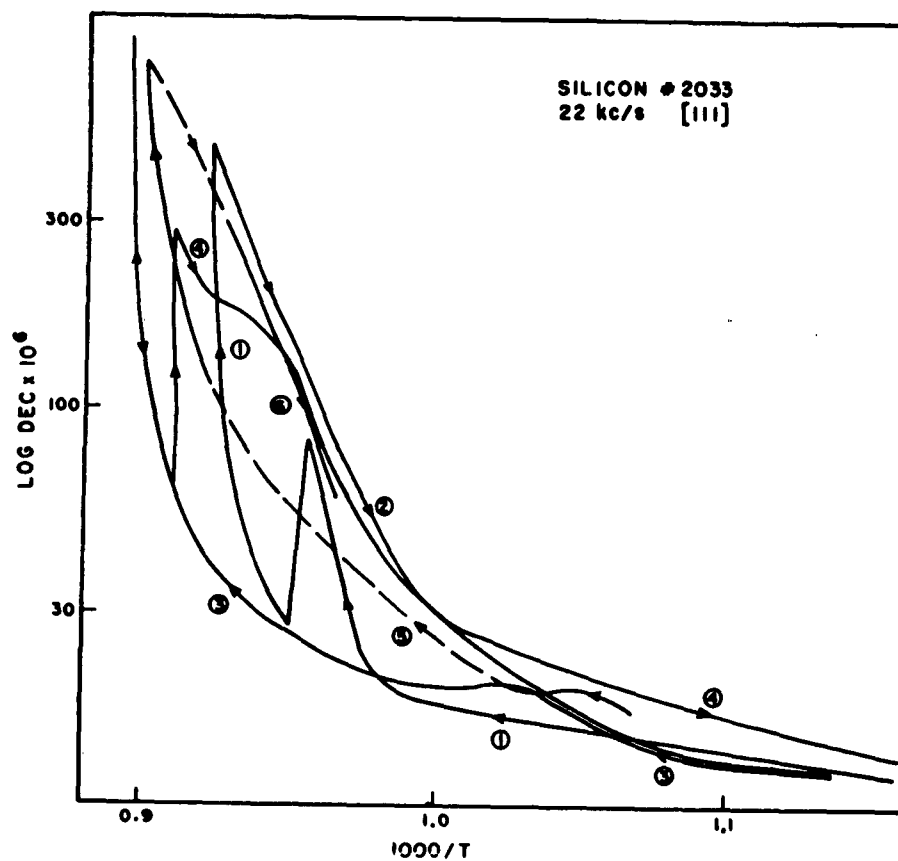


FIG. 30 - INTERNAL FRICTION OF SILICON 2033:  
SHOWING HEATING AND COOLING SEQUENCE

$$\nu = B e^{F_1}$$

where

$$F_1 = - \frac{4.68 W_k}{kT} + 3.9$$

in the region in which we are interested. The parameter B has the value

$$\frac{\pi^2}{32} \frac{Gb^2}{a^2 \nu^2} \frac{kT}{m^{3/2} E_0^{1/2}}$$

m and  $E_0$  being the mass and energy per unit length of the dislocation. In silicon, the value of B is thus of the order of  $5 \times 10^{10}$  at 1000°K. Consistently with the theory,  $E_0$  is interpreted as being the energy of the elastic strain field only; the core is excluded. This estimate of B could be out by a factor of 3.

Now, fitting the experimental value  $1.6 \text{ eV} = 4.68 W_k$ , we find that the dislocation relaxation frequency is of the order of 30 kc/s at 720°C, and hence a maximum would be expected at this temperature. The absence of such a maximum throws doubt on the validity of the theory.

The value of kink energy is given by

$$W_k = \frac{4}{\pi} \left( \frac{K}{\pi} \frac{a}{b} \right)^{1/2} Gb^2 a$$

If we take  $E_0 = Gb^2$ , and put the Peierls force = KG. The Peierls force may be regarded as the difference between the maximum and minimum dislocation core energies, multiplied by a factor  $\pi/ab$ . Since  $Gb^2 = 32 \text{ eV}$  in silicon, we have  $K = 2.2 \times 10^{-4}$ , which is fairly close to the value found in fcc metals. Since bonding in silicon is highly directional, one would expect a much larger value of K, and hence interpretation along the lines of the SDP theory does not seem correct in this respect either.

Brailsford's theory gives, for a single dislocation of length  $L$ ,

$$\Delta_d = \Delta_1(L, T) \omega \tau_L / (1 + \omega^2 \tau_L^2)$$

The modification of the theory discussed in Appendix IV shows that  $\tau_L = L^2 / D' \pi^2$ ,  $D'$  being an effective kink diffusion constant (along the dislocation line). Substitution of reasonable values, assuming in this case that the experimental value 1.6 eV is the activation energy of kink diffusion, indicates that below about 1000°C,  $\omega \tau \gg 1$  at 30 kc/s. This is equivalent to saying that kinks diffuse only a fraction of  $L$  along the dislocation line during each cycle. If we then assume the temperature is below this value, a considerable simplification occurs in the integration over all dislocations, since the contribution of each section is proportional to its length. Substitution of the value for  $\Delta_1(L, T)$  gives

$$\Delta_d = \frac{8 G a^2 b^2 \mu p_o L}{\pi V k T \omega}$$

where  $V$  is the specimen volume,  $\mu$  the mobility, and  $p_o$  the kink density. It is a reasonable assumption, for all but extremely low angles between the dislocation and the lattice plane, that thermally generated kinks can be neglected: so that  $p_o = \tan \theta / a$ . Integrating over all dislocations is now only a matter of summing the lengths, and we obtain directly the result of Appendix IV. The value predicted from this result must be multiplied by a factor of order 0.4 to account for orientation effects, giving a final value of  $8 \times 10^{-8}$  for  $\Delta f/N$ . This is close to the values given in the last column of Table 2. Hence, if the Brailsford theory is applicable, the average built-in kink density should be close to that assumed in the appendix, that is, about 1 every 20 atom distances. Such a density seems reasonable, and is in agreement with infra-red photographs of Dash<sup>17</sup> which show only small angles between dislocations and the lattice planes.

The flattening of the 3 kc/s curve of Figs. 25 and 26 may be taken as indicating the approach to a maximum where  $\omega \tau_L = 1$ . A more marked flattening occurs after a short anneal. At the highest

temperature, as would be expected from increased pinning of dislocations and consequent shortening of  $\tau_L$ . If the maximum is assumed to occur near 1050°C, then the mean dislocation length  $l_0$  can be derived from  $\tau = 10 l_0^2 / D' \pi^2$ . The factor 10 arises, as shown by Brailsford, if we assume an exponential distribution of dislocation lengths rather than a constant value. Substituting the expression for  $D'$  given in Appendix IV gives  $l_0 = 5 \times 10^{-5}$  cm. This value is of the order of that expected if the dislocations are in the form of a network and pinned at intersections, although this does not necessarily show that this, rather than impurity pinning, is dominant.

Hence, the orders of magnitude of theory and experiment are sufficiently in agreement to indicate that the abrupt kink theory is quite possibly applicable. Certainly, the model is of the kind to be expected a priori: the discrete nature of the bonding should lead to a sizable activation energy for kink diffusion. A further check could be made by studying dislocation pinning by impurities since, at temperatures below 1000°C, the internal friction should not be sensitive to the location of pinning points further apart than about  $10^{-6}$  cm. Careful design of pinning experiments is required since the total density of pinning points required to demonstrate an effect is very low, of the order of  $10^{13}$  per  $\text{cm}^3$ , and it would be easy to saturate this value.

## Section VII

### INTERNAL FRICTION OF SILICON CARBIDE

Several series of measurements have been made on a pale green transparent silicon carbide crystal, of dimensions  $0.95 \times 1.40 \times 10.23$  mm, resonating at 110 kc/s. The specimen axis was  $[11\bar{2}0]$ , in the hexagonal plane. Contrary to expectation, considerable variations in internal friction have been observed below 900°C. This variation was sometimes erratic in nature, although several consistent features were observed. The effect of a heat to 910°C, followed by annealing at 820°C for 50 min. and a subsequent cooling is shown in Fig. 31. The internal friction appears to rise continuously during anneal at an elevated temperature. Figure 32 shows the unrepeatable nature of the behavior between 5° and 140°C.

A consistently observable peak at 500°C is shown in Fig. 33; it has an initial height of  $1.6 \times 10^{-5}$ , is increased after 50 min. at 820°C, decreased after 4 hrs. at 265°C, and restored to its previous maximum after heating to 1070°C. The width of this peak is greater than that to be expected from simple point defect relaxation, but may well be due to relaxation of a center of a slightly more complicated nature which has two or more relaxation times. If this is the case, all the activation energies should be close to 1.4 eV, assuming the

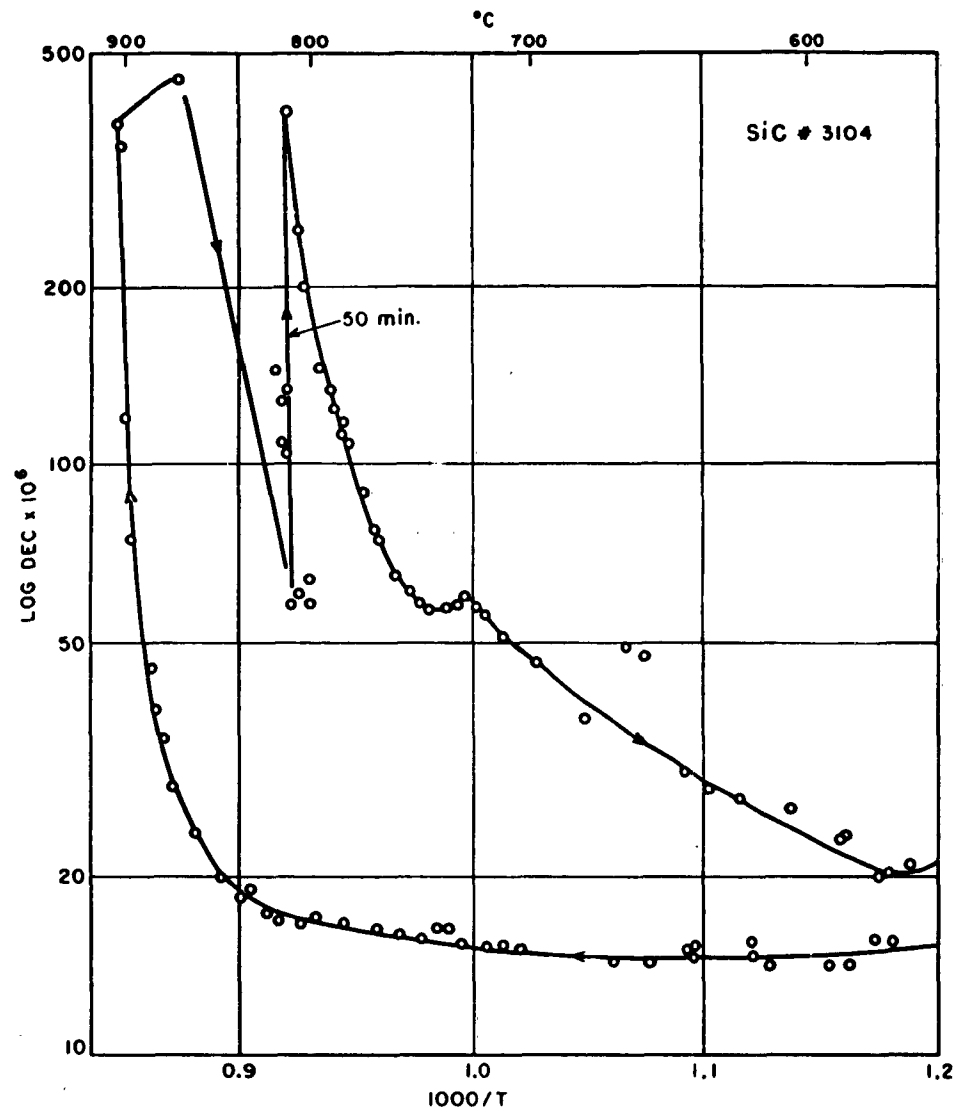


FIG. 31 - INTERNAL FRICTION OF SILICON CARBIDE 3104:  
HIGH TEMPERATURE RISE

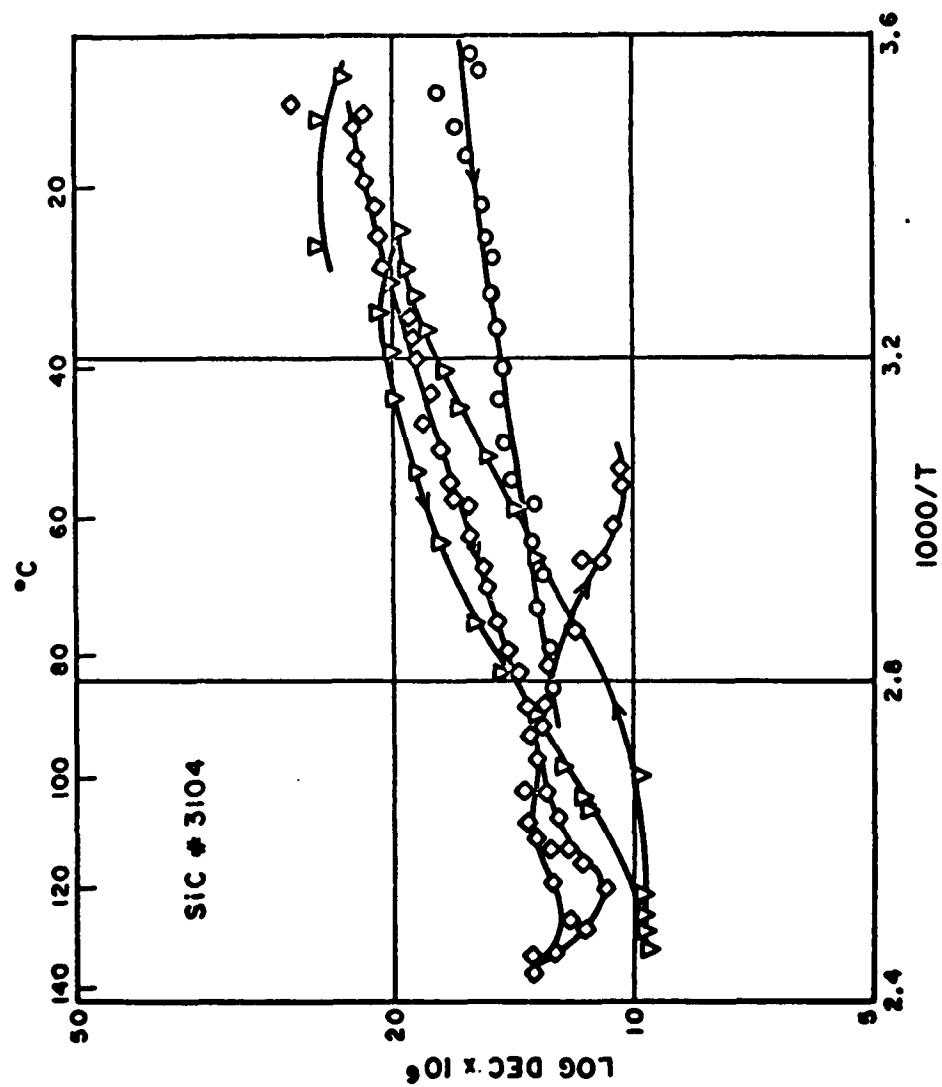
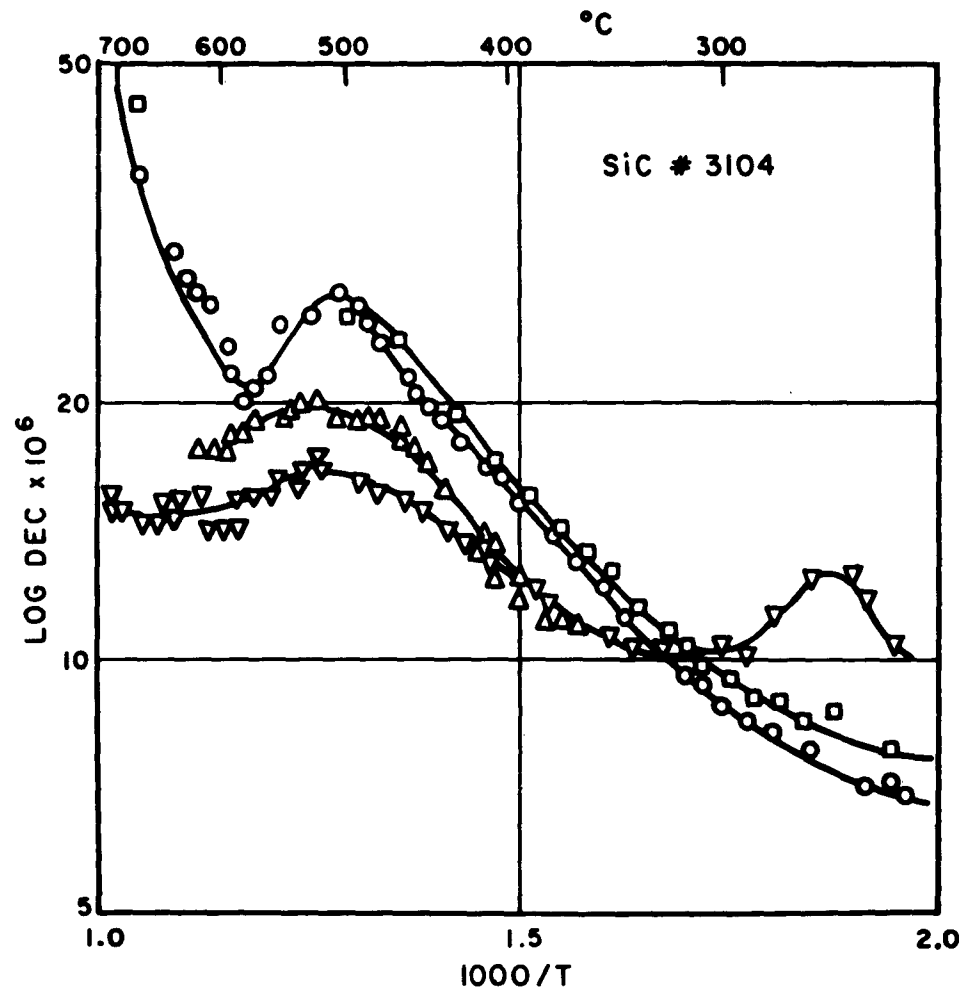


FIG. 32 - INTERNAL FRICTION OF SILICON CARBIDE 3104:  
LOWER TEMPERATURE VARIATION

Sequence of heating: ① ② ③





**FIG. 33 - INTERNAL FRICTION OF SILICON CARBIDE 3104:  
500°C PEAK**

- ▼ Initial cool after 5 min. at 780°
- After heating to 910° and holding for 50 min. at 810°
- ▲ After 6 hrs. at 265°
- After 95 min. at 1050°

normal expression for jump rate. This energy is much less than that of substitutional diffusion, and may possibly be associated with interstitial defects. The thermal behavior is not easy to understand, and requires more investigation. Possibly the defect becomes bound more firmly in the lattice at the lower temperatures, and freed at higher temperatures. Internal precipitation may be involved.

The behavior at high temperatures is very similar in appearance to that in the anomalous silicon sample 2033. Possibly similar dislocation effects are occurring. No firm hypothesis can be made until comparative studies of several samples have been made, and the dislocation distributions observed by etch pit methods. The variation at room temperature cannot be readily identified with any known process.

Thermoelastic relaxation<sup>1</sup> can be eliminated as a possible process, since the relaxation time for a specimen of this thickness is of the order of one second, much longer than the oscillation period. Damping due to coupling to charge carriers via the deformation potential should be very small, since the density of intrinsic charge carriers is very small due to the large band gap. A further possible source of damping is that due to piezoelectric coupling.<sup>3</sup> However, although there is probably some piezoelectric effect in silicon carbide for stresses along the hexagonal axis, the symmetry of any of the polytypes is such that stresses in the hexagonal plane will not produce a piezoelectric effect.

## Section VIII

### INTERNAL FRICTION OF ZINC OXIDE

One crystal of zinc oxide has been studied. It was 0.98 mm across, 1.3 cm long, clear and colorless, and was measured in flexural oscillation, 0.006" holes being drilled through the nodal planes, from one corner to the other of the hexagon. The oscillation frequency was 29 kc/s, and the axis of the specimen was the hexagonal crystal axis. Considering the small size of the specimen, the background damping due to the support wires is surprisingly low, being estimated at a log. dec. of  $2 \times 10^{-6}$ . Higher values of background damping have been seen in some regions: these are amplitude dependent, erratic in magnitude, and are clearly due to slipping of the wires. Points having any appreciable amplitude dependence are omitted from the data. A further possible source of error, which can produce a systematic amplitude dependence, is the coupling between the closely spaced modes of a slightly imperfect hexagonal bar. No evidence of this occurrence is seen.

Figure 34 shows the temperature variation of log. dec. between 30 °C and 800 °C. It is evident that the thermal treatment has changed the magnitude of the processes occurring between the first and second heating and between the second and third. The third heating was only to 300 °C, and this produced no change, the fourth run overlapping exactly. There is an indication that annealing is occurring fairly rapidly at the highest temperature of the second heat, since the points taken during cooling lie below the points taken a few minutes before, during heating. For the initial heating, a large amplitude dependence of damping occurred and hence points are not shown, while for the cooling, points were taken at too widely spaced intervals to make a continuous curve. However, it can be seen that in this case some changes have taken place below 300 °C between first cooling and second heating.

No interpretation of these curves can be given at present. It is evident that the peaks are not due to simple point defect relaxation since they are at least twice as broad as would be expected. Again, a more complex relaxation with a narrow range of relaxation times may be involved. One possible mechanism producing loss is the motion of a zinc vacancy around an ionized impurity. A recent paper by Azaroff<sup>18</sup> argues that the motion of a zinc atom from a normal site into an interstitial position would require an energy of about 1.7 eV, and the activation energy of motion of a zinc vacancy should be of the same order, even when associated with a charged impurity. This would lead to a peak around  $1000/T = 1.0$ , on the usual assumption that  $\tau_0 \sim 10^{-13}$  sec. Thus the rise observed at the higher temperature may represent the beginning of a peak due to this mechanism. It is tentatively assumed that the changes in the other peaks represent changes of magnitude rather than position. The peak at  $1000/T = 1.65$  appears not to be changed by heat treatment, while the one at 130 °C decreases and a further one appears at 200 °C. This latter assumption is made on the basis of the small lump appearing on the low-temperature shoulder of the last curve, and will require confirmation.

Again, thermoelastic relaxation and damping due to coupling with the deformation potential can be eliminated as significant processes, as in silicon carbide. Piezoelectric coupling, however, is large, the piezoelectric coupling coefficient having been shown by Hutson<sup>19</sup> to be  $K = 0.4$ , 4 times as large as that of quartz. The theory of Hutson and White<sup>3</sup> shows that the log. dec. due to piezoelectric coupling is

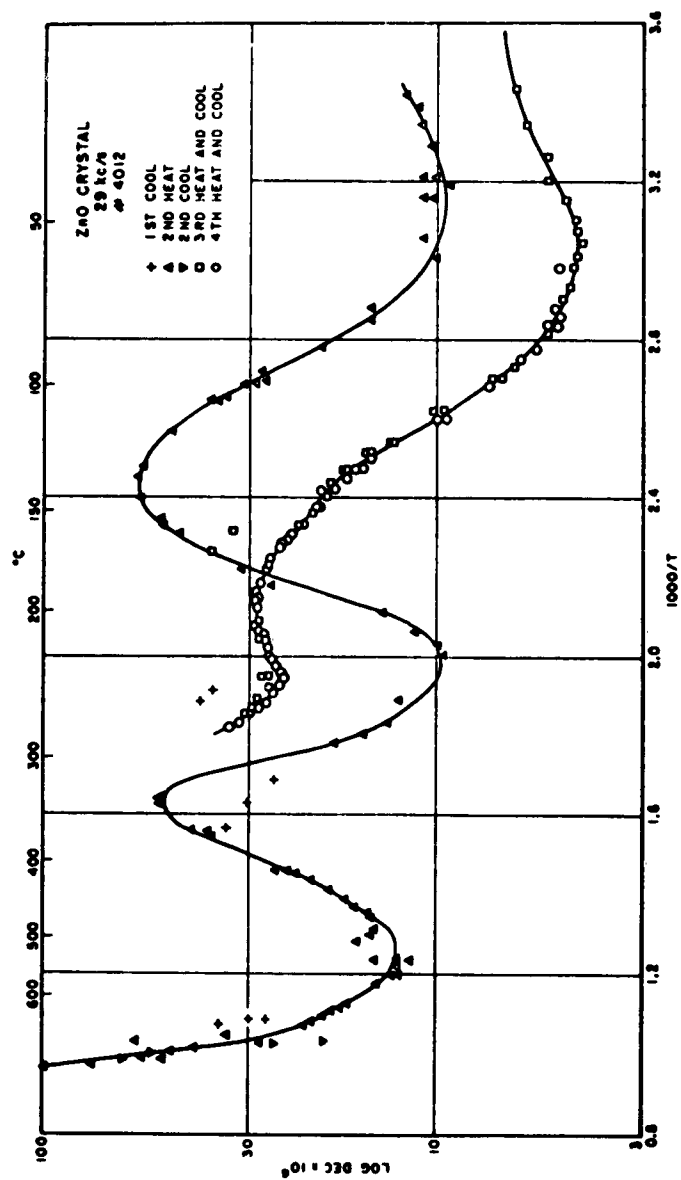


FIG. 34 - INTERNAL FRICTION OF ZINC OXIDE

$$\Delta = \frac{K^2 \omega_c / \omega}{1 + 2 \omega_c / \omega_D + (\omega / \omega_D)^2 + (\omega_c / \omega)^2}$$

where  $\omega_c$  = conductivity/dielectric constant, the dielectric relaxation frequency, and  $\omega_D$  is a diffusion frequency, of order  $10^{10}$ .

Thus, for the damping to be appreciable,  $\omega$  must be of the same order of magnitude as  $\omega_c$ . This will only occur in very high resistivity material, of the order  $10^5 \Omega$ -cm. Measurements on the specimen show resistivities of the order  $100 \Omega$ -cm, and hence this mechanism of damping also can be eliminated in this case.

## Section IX

### ELASTIC MODULI

Measurements of the frequency of oscillation allow the Young's modulus of the specimens to be calculated. The flexural oscillation technique is not ideal for the purpose, since the frequency varies as the square of the bar thickness, which can only be measured to an accuracy of a few percent. A far greater accuracy could have been obtained by using longitudinal oscillations, but the frequency of these oscillations, for the zinc oxide and silicon carbide specimens, would be well outside the present range of the apparatus. Full determination of all elastic constants requires the use of ultrasonic pulse-echo techniques, so that measurements can also be made under shear conditions. In silicon, a comprehensive study has already been made.<sup>20</sup>

The formula of Rayleigh<sup>21</sup> gives the Young's modulus for a bar in flexural vibration as

$$E = \alpha \rho \left( \frac{8}{9\pi} \frac{f l^2}{r_o} \right)^2$$

$f$  is the frequency,  $l$  the length, and  $r_o$  the radius of gyration of the cross-section.  $\alpha$  is an inertial correction factor, unity for a thin bar, which may be obtained from tables computed by Hasselman.<sup>22</sup> The tables refer to a rectangular section bar, and so we approximate the hexagonal section of the zinc oxide bar by a rectangular section of width 0.8 times that of the hexagon. Values of  $\alpha$  are then 1.035 for the zinc oxide specimen and 1.060 for silicon carbide. The derived values of Young's modulus at 0°C are  $1.56 \times 10^{12}$  dyne cm for ZnO [0001] and  $4.6 \times 10^{12}$  dyne cm<sup>-2</sup> for SiC [1120], with a probable error of 10 percent. The value for SiC may be compared with the polycrystalline value<sup>23</sup> of  $4 \times 10^{12}$  dyne cm<sup>-2</sup>.

The temperature coefficient of Young's modulus derived from frequency shift measurements is much more accurate than the absolute value of the modulus. However, thermal expansion values are needed, and these are not known at present. If  $\alpha$  is the linear expansion coefficient,  $\beta$  the modulus coefficient, and  $\gamma$  the frequency coefficient (all positive), then

$$\beta = \alpha + 2\gamma.$$

Figure 35 shows measurements of the frequency shift for silicon, silicon carbide, zinc oxide, and magnesium oxide. The elastic modulus shift will be about 2.2 times this in each case. It is notable that as the ionicity of the structure increases, the effect of temperature becomes more marked. Presumably the effect of crystal orientation is about the same for ZnO and SiC as it is for Si.

An unexpected frequency-shift effect, which is still not understood, has been observed at room temperature. Several silicon specimens have shown the effect. Typical is specimen 2043. After an initial heating to 1050°C it was cooled and held at room temperature for 64 hours. A drop in resonant frequency of 0.05 percent was seen which could have been due to removal of a surface layer 0.2 microns thick during the heating. However, on further measurement at room temperature, a further drop of 0.04 percent in frequency occurred, apparently produced by the conditions of measurement. Independent checks showed that this was a genuine change of frequency and not due to instrumental error. There are two conceivable sources of the shift: dislocation motion in the material, and the torque due to the support wires. Both of these can be almost certainly eliminated. The modulus defect due to dislocations can be shown to be of the order  $NL^2/6$ , where  $L$  is the unpinned dislocation length, if the dislocations are completely undamped and restrained only by their line tension. For  $L = 10^{-4}$  cm, a density of undamped dislocations of  $6 \times 10^5 \text{ cm}^{-2}$  would be sufficient to account for the observed deficit; but it is extremely unlikely that dislocations can be freed from damping forces at room temperature, particularly in view of the model of dislocation damping discussed in Section VI, part 2. As for the effect of the mounting wires on the resonant frequency, this is very small: the torsional rigidity of the wires can only change the frequency by 1 in  $10^{10}$ , while off-nodal location of 0.1 mm will cause a shift of only 1 in  $10^8$ . Hence the origin of the observed shift remains unexplained.

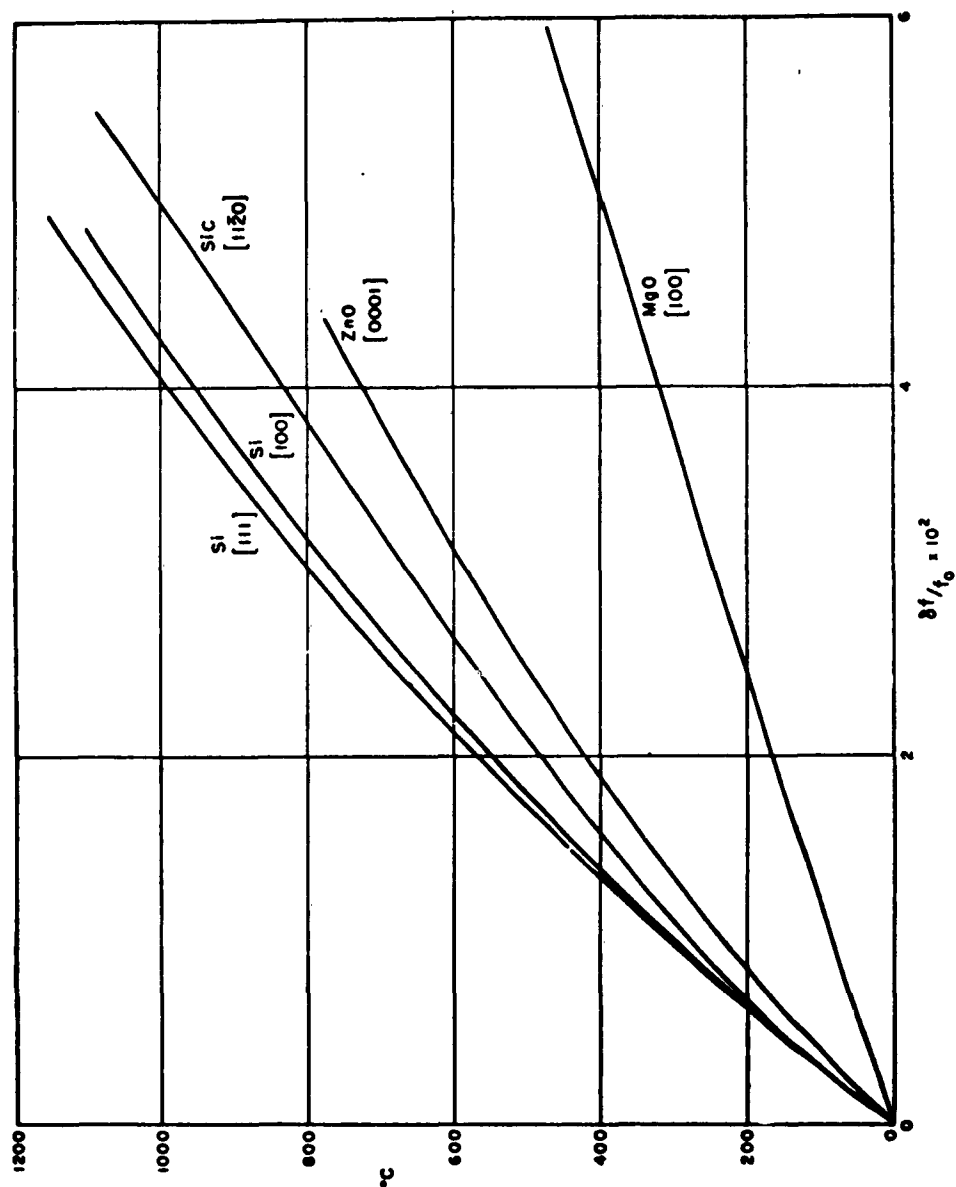


FIG. 35 - TEMPERATURE VARIATION OF ELASTIC MODULUS:  
SILICON, SILICON CARBIDE, ZINC OXIDE,  
MAGNESIUM OXIDE



## Section X

### CONCLUSION

It is difficult, in examining dislocation motion by internal friction methods, to positively identify any particular relaxation peak as due to a particular mechanism. Rather, the accretion of evidence of the effect of different parameters: frequency, dislocation content, purity: must be used to discriminate between different possible theories. The results on deformed pure silicon crystals given in this report show that the Brailsford abrupt-kink theory of dislocation motion fits the facts very closely, while pronounced discrepancies arise when other possible theories are considered. The result of identifying the observed dislocation damping with the abrupt-kink theory then allows assignment of a value  $1.61 \pm 0.02$  eV for the activation energy of kink motion. Further work is required to substantiate this identification; in particular, the effect of impurity content calls for investigation. The model is also rather simple as applied here, and it is possible that the small discrepancies which have been observed at the lower temperatures may be due to a more complicated situation, such as the presence of different types of kinks and different kinds of dislocation.

It has not been possible to analyze the unrepeatable and hysteretic behavior of the specimen which yielded by a localized shear process. It is possible that the local high densities of dislocations caused a continuous breaking-loose of highly mobile dislocations lying at a steep angle to the lattice plane; and it is equally possible that the high dislocation densities produced gross defects such as microcracks which showed variable behavior.

Creep observations made during the plastic deformation of silicon have been surprisingly variable. The source of this variation has not been identified, as some difference in either surface treatment, bar thickness, applied load, and rate of loading was present between all specimens. It appears that there is a considerable sensitivity of the creep behavior to most of these parameters. Incubation time, creep rate, and hardening behavior all varied in an apparently complicated manner, and comparison with previous work on germanium was not possible. However, a satisfactorily uniform dislocation density was produced in all but the one specimen which yielded in shear.

The measurements of silicon carbide and zinc oxide are essentially preliminary in nature. An unexpectedly large number of peaks in the internal friction of these materials appear between room temperature and 900°C, but it has not proved possible to analyze these. They are not due to simple diffusion of single interstitial atoms, as the width of the peak is too large. A more complex type of defect is indicated. It has been assumed that dislocation motion was very limited until higher temperatures were reached, since it has not been shown possible to

plastically deform either material below 1500°C. However, this hardness may not be intrinsic to the isolated dislocation, but a function of pinning, and the possibility of observable dislocation relaxation below 900°C cannot be ruled out at this stage. Further investigations on deliberately deformed crystals, and studies of the anneal behavior are required to identify the mechanisms producing the peaks.

# APPENDIX I

## FORCE AND ENERGY RELATIONSHIPS FOR A DISLOCATION CONTAINING KINKS

The model to be discussed here is based on the division of the total energy of a dislocation into two parts, the core energy, and the stress field energy. The core energy is contained in the rod of material of radius approximately one Burgers vector immediately surrounding the dislocation, while the stress field energy is contained in a hollow tube surrounding the core and of maximum radius of the order of the distance of the neighboring dislocations. We picture the dislocation as lying along simple lattice directions, deviations of the average dislocation line from this direction being made by relatively abrupt kinks. The assumption is now made that the stress field energy is that of the tube which follows the average dislocation direction, and is computed from elastic continuum theory, while the core energy is vested entirely in the bonding rearrangements in the core, and is not related to continuum concepts, so that energetic interactions between kinks do not occur. Figure 36 indicates the type of division being considered. An alternative, but apparently equivalent, model is discussed in Appendix III. The model has been formulated on partly intuitive grounds; a rigorous justification would be a formidable task, requiring accurate computation of the non-linear elastic effects close to the core and of the electron wave functions involved in the valency rearrangements at the core.

We further consider only the case in which thermal activation of kink pairs is negligible, and all kinks are of the same kind: following the notation of Brailsford,<sup>8</sup> p-type. The ends of the dislocation are pinned, so that the total number of kinks remains constant. Hence the kink energy is not relevant in any energetic interactions between the kinks and the dislocation stress field.

Let the kink density, measured in the lattice plane direction, be  $p$ . Let a force be applied to the dislocation and let the kinks move a distance  $x_1$ . If there is a force  $f$  on each kink due to damping of its motion, then the total work done per unit length along the  $x$ -axis

$$W = f p x_1$$

The dislocation moves  $x_1 \sin \theta$  normal to its axis, where  $\theta$  is the angle between the dislocation and the  $x$ -axis. If a force  $F$  per unit length of dislocation is applied normal to the dislocation, we have the energy relationship

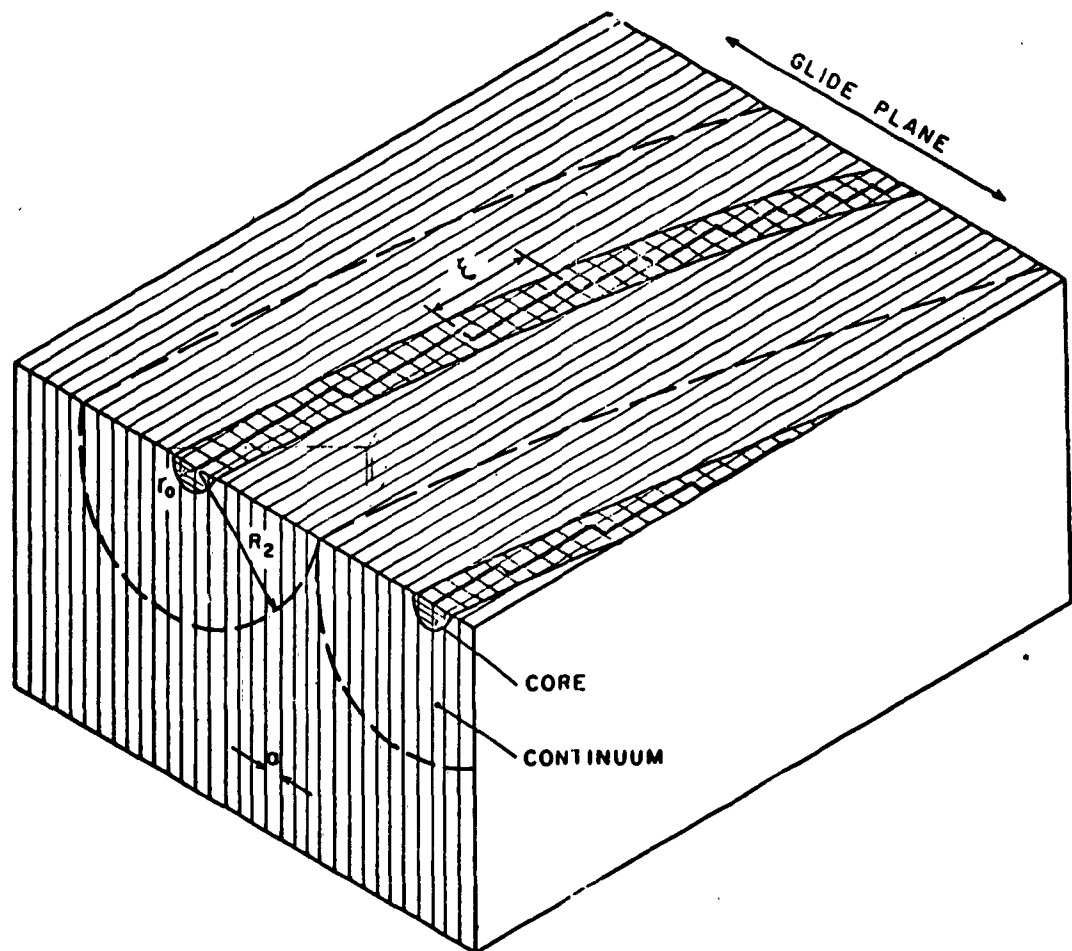


**FIG. 36 - KINKED DISLOCATION SHOWING CORE AND STRESS-FIELD REGIONS**

$$\frac{F}{\cos \theta} x_1 \sin \theta = f p x_1$$

Hence  $f = Fa$  since  $\tan \theta = pa$ .

If the dislocation line is curved, and the stress field energy is  $E_0$  per unit length, then  $F = E_0/\text{radius of curvature}$ ,

$$f = -E_0 a \frac{\partial^2 y}{\partial x^2} \bigg/ \left( 1 + \left( \frac{\partial y}{\partial x} \right)^2 \right)^{3/2}$$

where  $y$  is the dislocation displacement.

A more detailed calculation of energy changes on a virtual work basis can be used to check the validity of this stretched-string approach. Ideally, the fact should be considered that  $E_0$  changes a little as the kink density increases and the dislocation changes from pure edge to part screw (or vice versa); but the effect of this change will be relatively small.

## APPENDIX II

### DISLOCATION LINE TENSION IN THE BRAILSFORD THEORY

Brailsford shows that, if the thermal generation of kink pairs is the major limiting process involved in dislocation motion, and the stress-field energy discussed in Appendix I is neglected, "an analogy with an extensible string is alien to the concepts contained in the present model". The basis for this statement is that the energy of the extra thermally activated kinks produced when the material is stressed does not equal a hypothetical line tension, derived from the shape of the bowed line, multiplied by the gross increase in line length. While this is certainly true, the argument cannot immediately be applied to the internal friction theory, which depends on damped motion of built-in kinks, rather than thermally generated kinks.

It will now be shown that there is a way of formulating the line tension which is alternative to that given in Appendix I. In Appendix I, the core was taken to follow the mean dislocation direction. However, we may alternatively reduce the core diameter so that it has to follow the exact dislocation line. Now, the length of the core does not

depend on kink distribution, and the stress-field energy cannot be simply regarded as changing by virtue of the dislocation core length changing. Changes of stress-field energy will arise from its self-interaction, which can be formulated by considering the mutual repulsion of the kinks which will now have stress-fields in their own right. Such a repulsion will give an increase of energy if the kinks in the existing line are redistributed by an applied stress, in the following manner. Let the repulsive force be represented by an energy parameter  $\epsilon_r$  such that the total line energy is

$$W = E_0 L + \epsilon_k \int_0^L p \, dx + a \epsilon_r \int_0^L p^2 \, dx \quad (2.1)$$

$p$  being the kink density,  $\epsilon_k$  the kink energy, and  $a$  the spacing of the lattice planes.

If we now consider a steady-state condition then the total force due to the repulsion on a row of kinks per unit length

$$\begin{aligned} F &= - \frac{\partial W_{\text{repul.}}}{\partial x} = - \frac{\partial}{\partial x} (a \epsilon_r p^2) \\ &= - 2 a \epsilon_r \frac{\partial p}{\partial x} p \end{aligned}$$

and hence the force per kink is  $- 2 a \epsilon_r \frac{\partial p}{\partial x}$ .

The force on a kink due to an externally applied shear stress  $\sigma$  is  $\sigma ab$ . Under steady-state conditions, the flux of kinks due to the externally applied shear stress is balanced by both the back-diffusion under the concentration gradient and, on this model, the flux due to kink repulsion:

$$\mu p \sigma ab = D \frac{\partial p}{\partial x} + \mu p \cdot 2 a \epsilon_r \frac{\partial p}{\partial x}$$

where  $\mu$  is the kink mobility and  $D$  the diffusion constant. Since

$$\frac{\partial y}{\partial x} = -ap \quad (2.2)$$

$$\text{we have } D \frac{\partial^2 y}{\partial x^2} = \mu \sigma ab \frac{\partial y}{\partial x} + 2 \epsilon_r \mu \frac{\partial y}{\partial x} \frac{\partial^2 y}{\partial x^2} \quad (2.3)$$

$$\text{Now, putting } y = -a p_0 x + y_1 \quad (2.4)$$

and ignoring second-order terms

$$\left( \sigma \frac{\partial y_1}{\partial x}, \frac{\partial^2 y_1}{\partial x^2}, \frac{\partial y_1}{\partial x} \rightarrow 0 \right)$$

gives a dislocation line of constant curvature

$$\frac{\partial^2 y_1}{\partial x^2} = - \frac{a^2 p_0 \mu b \sigma}{D + 2 \epsilon_r \mu a p_0} \quad (2.5)$$

Comparing this with the formula for the curvature of a string of line tension  $S_1$  with a force  $\sigma b$ /unit length applied

$$S_1 \frac{\partial^2 y_1}{\partial x^2} = - \sigma b$$

shows that, if an analogy between the kink-repulsion and the line tension model is to be made,

$$S_1 = \frac{1}{a} \left[ 2 \epsilon_r + \frac{D}{\mu} \cdot \frac{1}{a p_o} \right]$$

The energy given to a line-tension dislocation by an applied stress  $\sigma$  is

$$\delta W = \frac{1}{2} \sigma b A = \frac{1}{2} \sigma b \int_0^L y_1 dx \quad (2.6)$$

where A is the area under the bowed-out dislocation loop. We now compare this with the change of energy derived from the kink repulsion formula (2.1)

$$\delta W_k = a \epsilon_r \left( \int_0^L p^2 dx - p_o^2 L \right)$$

from (2.2) and (2.4)

$$p = p_o - \frac{1}{a} \frac{\partial y_1}{\partial x}$$

and noting that, since  $y_1 = 0$  at  $x = 0, x = L$ ,

$$\int_0^L \frac{\partial y_1}{\partial x} dx = 0$$

$$\text{and} \quad \int_0^L \left( \frac{\partial y_1}{\partial x} \right)^2 dx = \int_0^L \left[ \frac{\partial y_1}{\partial x} y_1 \right] - \int_0^L \frac{\partial^2 y_1}{\partial x^2} \cdot y_1 dx$$



$$\int_0^L \left( \frac{\partial y_1}{\partial x} \right)^2 dx = - \frac{\partial^2 y_1}{\partial x^2} \int_0^L y_1 dx \text{ for constant curvature.}$$

then

$$\delta W_k = - \frac{\epsilon_r}{a} \cdot \frac{\partial^2 y_1}{\partial x^2} \cdot A$$

$$= \frac{1}{2} \sigma b A \frac{2 \epsilon_r a p_o \mu}{D + 2 \epsilon_r a p_o \mu} \quad \text{from (2.5)}$$

Comparison of this expression with (2.6) shows that not all the energy of deformation is stored as kink interaction energy. The remainder is transferred to thermal energy of the lattice. However, unless the frequency of oscillation is very high, the transfer process is isothermal, and hence the energy is recoverable when the deforming stress is removed. Thus the extensible-string analogy is not rendered invalid by this difference between the energy given to the dislocation system and that stored in the kink repulsion fields. If the kink repulsion is sufficiently large, the effective line tension is

$$S = \frac{2 \epsilon_r}{a} \quad (2.7)$$

### APPENDIX III

#### COMPARISON OF KINK REPULSION AND STRESS-FIELD LINE TENSION MODELS

In Appendix II it was shown how kink repulsion would give rise to a line tension type of force. The equivalence of kink repulsion to line tension will now be illustrated; again, rigorous proof would require very detailed computation.

On the kink repulsion model, the axis of the stress field is considered to be located exactly at the core. Hence its total length does not depend on the kink distribution. However, the kinks now have stress fields associated, and since the kinks are parallel, the fields will cause repulsion. The close analogy between electromagnetic current interactions and dislocation interactions show that the stress field of an element of dislocation is given by

$$E_1 \frac{\cos \phi \, dx}{r^2}$$

Integrating this and equating the total to that given by Cottrell for the field (in the glide plane) of a straight dislocation shows that the constant multiplier  $E_1$  has the value

$$\begin{aligned} Gb^2 / 4\pi (1-\nu) \quad (\text{edge}) \\ . Gb^2 / 4\pi \quad (\text{screw}) \end{aligned} \tag{3.1}$$

$G$  being the shear modulus,  $\nu$  Poissons ratio,  $b$  the Burgers vector.

If one now regards the kinks as being dislocation elements perpendicular to the average dislocation line, then the repulsive force between any pair is  $f_r = E_1 a^2 / \xi^2$ . This form is consistent with the energy equation (2.1), whether the total interaction between kinks or nearest neighbor interactions only are considered. Considering now the total line energy due to repulsive forces, we have an energy per kink of

$$\frac{E_1 a^2}{\xi} \sum_{1}^{R_1 p} \frac{1}{n} \quad (3.2)$$

in a line of uniform density. A cut-off length  $R_1$  must be specified to prevent the energy becoming infinite.

Now, taking the other viewpoint, and considering a line energy per unit length  $E_0$  along the dislocation, the change of energy on introducing kinks is

$$\begin{aligned} \delta W/L &= E_0 \tan \theta - E_0 \\ &= E_0 \frac{a^2 p^2}{2} \text{ for small } \theta. \end{aligned} \quad (3.3)$$

and hence the change of energy per kink is  $E_0 a^2 p^2/2$ . Identifying the two viewpoints, and equating (3.2) with (3.3) we have

$$E_1 \sum_{1}^{R_1 p} \frac{1}{n} = \frac{E_0}{2}$$

If the dislocation is pure edge, the line energy is

$$E_0 = \frac{Gb^2}{4\pi(1-\nu)} \ln \left( \frac{R_2}{r_0} \right)$$

$R_2$  and  $r_0$  being outer and inner cut-off radii. Inserting the value of  $E_1$  from (3.1) for the screw-type kinks, we have

$$\sum_{1}^{R_1 p} \frac{1}{n} = \ln R_1 p + \gamma = \frac{1}{2(1-\nu)} \ln \frac{R_2}{r_0}$$

$\gamma = 0.5772$  (Euler's constant).

It is reasonable to put  $R_1 \sim R_2 \sim L$ . Taking  $\nu = 0.1$ , and putting  $r_0 = \alpha a$ , it emerges that

$$-0.5 < \ln \alpha < 0.5$$

The closeness of  $\alpha$  to unity shows that the inner cut-off radius will have a value near the lattice plane spacing, and hence the kink repulsion and stress-field line tension models are compatible numerically as well as conceptually. The lack of an exact identification reflects the uncertainty in the method of separating the core energy (independent of kink configuration) from stress field energy (dependent on kink configuration).

#### APPENDIX IV

##### MODIFICATION OF BRAILSFORD THEORY: STRESS-FIELD ENHANCED KINK DIFFUSION

If the stress-field is taken into account, as in Appendix I, the total driving force on a kink when a shear stress  $\sigma$  is applied perpendicular to the lattice planes is

$$F = \sigma ab + E_0 a \frac{\partial^2 y}{\partial x^2} / \left[ 1 + \left( \frac{\partial y}{\partial x} \right)^2 \right]^{3/2}$$

Setting up a dynamic kink equation identical to that of Brailsford

$$\frac{\partial y}{\partial t} + F\mu \frac{\partial y}{\partial x} - D \frac{\partial^2 y}{\partial x^2} = 0$$

(considering p-type kinks only), and putting  $y = -a p_0 x + y_2 e^{i\omega t}$  we have

$$\begin{aligned} & i\omega y_2 e^{i\omega t} + e^{i\omega t} \sigma_0 \mu ab \left[ -ap_0 + \frac{\partial y_2}{\partial x} e^{i\omega t} \right] \\ & + \frac{E_0 a \mu \frac{\partial^2 y_2}{\partial x^2} e^{i\omega t} \left[ -ap_0 + \frac{\partial y_2}{\partial x} e^{i\omega t} \right]}{\left[ 1 + (ap_0)^2 + 2 \frac{\partial y_2}{\partial x} ap_0 e^{i\omega t} \right]^{3/2}} - D \frac{\partial^2 y_2}{\partial x^2} e^{i\omega t} = 0 \end{aligned}$$

Now, eliminating second-order terms, the solution of the problem follows exactly as demonstrated by Brailsford, but with an enhanced diffusion term

$$D' = D + \frac{E_0 a^2 p_0 \mu}{\left[ 1 + (ap_0)^2 \right]^{3/2}}$$

If  $\theta = ap_0$  is small, and the Einstein relation  $D = \mu kT$  is assumed,

$$D' = D \left[ 1 + \frac{E_0 a}{kT} \theta \right]$$

The dislocation line energy per atom will be of the order  $Gb^2 a$ , 32 eV in silicon; and so a dislocation line having  $\theta = 0.05$  will show an

effective kink diffusion enhanced by a factor of about 18 over the value used by Brailsford. Following Brailsford, the relaxation time for a dislocation of length  $L$  is

$$\tau_L = \frac{L^2}{D' \pi^2}$$

and, for an exponential distribution of free dislocation segments, the maximum logarithmic decrement

$$\Delta_m = \frac{2.1 N}{10 \pi} 8 G a^2 b^2 \mu p_o \tau_e$$

occurs at

$$\omega \tau_e = 1$$

where

$$\tau_e = \frac{10 l_o^2}{\pi^2 D'}$$

for an exponential distribution of mean length  $l_o$ . Thus the effect of enhanced diffusion is to lower the expected temperature and magnitude of the peak.

Below the peak temperature  $\omega \tau \gg 1$ , the log. dec.

$$\Delta = \frac{8 G a^2 b^2 \mu p_o N}{\pi \omega}$$

To estimate the magnitude of the decrement one needs to estimate  $\mu$ . If the activation energy is  $H$ , then diffusion theory shows that an approximate value for  $\mu$  is

$$\frac{1}{kT} D_0 e^{-H/kT}$$

where

$$D_0 = z d^2 \frac{kT}{h} \sqrt{\left(\frac{m}{m^*}\right)} e^{S/k}$$

$z$  is the number of nearest-neighbor sites,  $d$  the atomic spacing along the dislocation line,  $m$  the atomic mass,  $m^*$  the effective mass of the kink, and  $S$  the entropy of diffusion. Studies of oxygen diffusion in silicon<sup>3</sup> have shown that the entropy term in this case is rather high, of the order of 20. A value of this order will be assumed for kink diffusion. Putting  $H = 1.61 \text{ eV}$ ,  $m/m^* = 1$ ,  $ap = 0.05$  gives an unexpected value for  $\Delta f/N$  of  $2 \times 10^{-7}$  at  $1000/T = 1.8$ .

## APPENDIX V

### COMPATIBILITY OF BRAILSFORD AND KGL THEORIES

The Koehler-Granato-Lucke theory<sup>4</sup> sets up the dislocation damping equation

$$A \frac{\partial^2 y}{\partial t^2} + B \frac{\partial y}{\partial t} - E_0 \frac{\partial^2 y}{\partial x^2} = b\sigma \quad (5.1)$$

for the dislocation displacement  $y$  due to applied stress  $\sigma$ . In the frequency range of interest, the first, inertial, term can be neglected. If we retain the model of Appendix I, then  $E_0$  can be identified with the stress-field energy per unit length, while the friction coefficient  $B$  can be derived from the kinetics of kink diffusion. The axes of (5.1) are taken in a slightly different direction from those of the other appendices; hence the  $x$ -axis passes through the dislocation pinning points rather than being parallel to the lattice planes.

If the kink density along the lattice plane is  $p$ , and the kinks move with velocity  $v$ , then the dislocation velocity parallel to the lattice planes is  $v \sin \theta$ , and the velocity normal to the dislocation is  $\partial y / \partial t = v \cos \theta$ . The kink velocity under a driving force  $f$  is

$$v = \mu f$$

If now the dislocation as a whole experiences a damping force  $F$  per unit length normal to the dislocation, the rate of energy dissipation per unit length is

$$\begin{aligned} F \frac{\partial y}{\partial t} &= f v p \cos \theta \\ &= \frac{v^2}{\mu} p \cos \theta \\ &= \left( \frac{\partial y}{\partial t} \right)^2 \frac{p \cos \theta}{\mu a^2 p^2 \cos^2 \theta} \end{aligned}$$

The term  $p \cos \theta$  in the first line is the kink density along the dislocation line. Thus, dividing by  $\partial y / \partial t$ , we find a damping constant  $B$  of value

$$\frac{1}{\mu a^2 p \cos \theta}$$

Substituting this value in the complete KGL theory and putting  $A \rightarrow 0$ , we obtain

$$\tau_L = \frac{BL^2}{\pi^2 E_0} = \frac{L^2}{\pi^2 \mu a^2 p_0 E_0 \cos \theta} \quad (5.2)$$



and

$$\Delta_0 = \frac{8 G b^2 L^2}{\pi^3 E_0 \cos^3 \theta} \quad (5.3)$$

if the justifiable approximation  $p \rightarrow p_0$  is taken at an appropriate stage. In the limit of small kink densities  $\cos \theta \rightarrow 0$ , and these formulae then become identical to those of the modified Brailsford theory (Appendix IV). Thus the thermally activated kink diffusion model is consistent with, and complementary to, the stretched string model. The formalism of dislocation length averaging and orientation correction developed by Granato and Lucke may be used in applying (5.2) and (5.3) to any particular situation.

## LIST OF REFERENCES

1. C. Zener, *Phys. Rev.* 53, 90, 1938.
2. G. Weinreich, *Phys. Rev.* 104, 321, 1956.
3. A. R. Hutson, D. L. White, *J. Appl. Phys.* 33, 40, 1962.
4. J. L. Snoek, *Physica*, 8, 711, 1941.
5. P. D. Southgate, *Proc. Phys. Soc. (London)* 76, 385, 1960.
6. P. G. Bordoni, *Nuovo Cimento (Suppl.)* 42, 43, 1960.
7. A. Seeger, H. Donth, F. Pfaff, *Disc. Farad. Soc.* 23, 16, 1957.
8. A. D. Brailsford, *Phys. Rev.* 122, 778, 1961.
9. A. Granato, K. Lucke, *J. Appl. Phys.* 27, 583, 1956.
10. J. S. Koehler, *Imperfections in Nearly Perfect Crystals* (J. Wiley, 1952) p. 197.
11. J. C. Swartz, J. Weertman, *J. Appl. Phys.* 32, 1860, 1961.
12. P. G. Bordoni, *Nuovo Cimento*, 4, 177, 1947.
13. P. D. Southgate, *J. Sci. Instr.* 36, 28, 1959.
14. W. R. Smythe, *Static and Dynamic Electricity* (McGraw-Hill, 1950) p. 105.
15. P. Penning, G. de Wind, *Physica*, 25, 775, 1959.
16. H. J. Queisser, *J. Appl. Phys.* 32, 1776, 1961.
17. W. C. Dash, *J. Appl. Phys.* 27, 1193, 1956.
18. L. Azároff, *J. Appl. Phys.* 32, 1663, 1961.
19. A. R. Hutson, *Phys. Rev. Letters*, 4, 505, 1960.
20. H. J. McSkimin, *J. Appl. Phys.* 27, 1219, 1956.
21. Lord Rayleigh, *Theory of Sound*, Vol. 1, p. 273.
22. D. P. H. Hasselman, *Tables of computation of elastic modulus*, Carborundum Co., Niagara Falls, 1961.
23. J. B. Wachtman, D. G. Lam, *J. Am. Ceram. Soc.* 42, 254, 1959.

Aeronautical Systems Division, Dir/Materials & Processes, Metals & Ceramics Lab, Wright-Patterson AFB, Ohio.  
Rpt No ASD-TDR-62-431. DISLOCATION MOBILITY & PINNING IN HARD MATERIALS THROUGH INTERNAL FRICTION STUDIES. Final report, Feb 63, 90pp incl illus, tables, & 23 refs.  
Unclassified Report

The internal friction of covalently bonded and partly covalently bonded materials is being investigated at elevated temperatures. The apparatus operates on the electrostatic drive system, and covers the range 0 to 1500°C, 1 to 200 kc/s. Single crystals of silicon, silicon carbide, and zinc oxide have

been measured. A steady rise of internal friction is seen in deformed silicon specimens above 500°C, which appears to be thermally activated with an activation energy of 1.61±0.02 eV. The rise is attributed to the dislocation damping; its magnitude is approximately proportional to the dislocation density and inversely to the frequency. Quantitative identification can be made with Brailsford's abrupt-kink theory of dislocation damping if a reasonable kink density is assumed, in which case the activation energy is that of kink mobility.

1. Deformation of Metals
2. Mechanical Damping
- I. AFSC Proj 7350, Task 735003
- II. Contract No. AF 33 (616)-8132
- III. Armour Research Foundation, Illinois
- IV. Southgate, P.
- V. Aval fr OTS
- VI. In ASTIA collection

Aeronautical Systems Division, Dir/Materials & Processes, Metals & Ceramics Lab, Wright-Patterson AFB, Ohio.  
Rpt No ASD-TDR-62-431. DISLOCATION MOBILITY & PINNING IN HARD MATERIALS THROUGH INTERNAL FRICTION STUDIES. Final report, Feb 63, 90pp incl illus, tables, & 23 refs.  
Unclassified Report

The internal friction of covalently bonded and partly covalently bonded materials is being investigated at elevated temperatures. The apparatus operates on the electrostatic drive system, and covers the range 0 to 1500°C, 1 to 200 kc/s. Single crystals of silicon, silicon carbide, and zinc oxide have

been measured. A steady rise of internal friction is seen in deformed silicon specimens above 500°C, which appears to be thermally activated with an activation energy of 1.61±0.02 eV. The rise is attributed to the dislocation damping; its magnitude is approximately proportional to the dislocation density and inversely to the frequency. Quantitative identification can be made with Brailsford's abrupt-kink theory of dislocation damping if a reasonable kink density is assumed, in which case the activation energy is that of kink mobility.

1. Deformation of Metals
2. Mechanical Damping
- I. AFSC Proj 7350, Task 735003
- II. Contract No. AF 33 (616)-8132
- III. Armour Research Foundation, Illinois
- IV. Southgate, P.
- V. Aval fr OTS
- VI. In ASTIA collection